Effect of flow-geometry on turbulence-scalar interaction in premixed flames

Y. Minamoto,[1] N. Fukushima,[1] M. Tanahashi,[1] T. Miyauchi,[1] T. D. Dunstan,[2] and N. Swaminathan[2]
[1]*Department of Mechanical and Aerospace Engineering, Tokyo Institute of Technology, 2-12-1 Ookayama, Meguro, Tokyo 152-8550, Japan*
[2]*Department of Engineering, University of Cambridge, Cambridge CB2 1PZ, United Kingdom*

(Received 19 April 2011; accepted 8 November 2011; published online 13 December 2011)

Turbulent combustion of stoichiometric hydrogen-air mixture is simulated using direct numerical simulation methodology, employing complex chemical kinetics. Two flame configurations, freely propagating and V-flames stabilized behind a hot rod, are simulated. The results are analyzed to study the influence of flame configuration on the turbulence-scalar interaction, which is critical for the scalar gradient generation processes. The result suggests that this interaction process is not influenced by the flame configuration and the flame normal is found to align with the most extensive strain in the region of intense heat release. The combustion in the rod stabilized flame is found to be flamelet like in an average sense and the growth of flame-brush thickness with the downstream distance is represented well by Taylor theory of turbulent diffusion, when the flame-brushes are non-interacting. The thickness is observed to saturate when the flame-brushes interact, which is found to occur in the simulated rod stabilized flame with Taylor micro-scale Reynolds number of 97. © *2011 American Institute of Physics*. [doi:10.1063/1.3665619]

I. INTRODUCTION

The scalar dissipation rate is a key quantity in turbulent combustion modeling and it represents the scalar mixing rate at small scales which are required to maintain combustion. In premixed combustion, this quantity signifies the average rate at which hot products and cold reactants mix at scales relevant to sustain combustion. This direct relationship was shown explicitly by Bray[1] and Libby and Bray[2] as

$$\bar{\dot{\omega}}_c \simeq \frac{2}{(2C_m - 1)} \bar{\rho} \tilde{\epsilon}_c, \tag{1}$$

for the mean reaction rate of the progress variable c, which is defined later. In the above equation, ρ is the fluid density, $\tilde{\epsilon}_c \equiv \overline{\rho \alpha_c (\nabla c'' \cdot \nabla c'')}/\bar{\rho}$ is the mean scalar dissipation rate of the progress variable Favre fluctuation, c''. The molecular diffusivity for the progress variable is denoted as α_c. The over-bar and tilde denote the Reynolds and Favre means, respectively. The C_m is the model parameter with a typical value of 0.7–0.8 for lean hydrocarbon- and ultra lean hydrogen-air flames.[3] Equation (1) is strictly valid when the flame front thickness is smaller than the Kolmogorov scale of the turbulence. This situation is typically known as flamelet combustion in general. However, this expression is sufficiently accurate even for thin reaction zones regime combustion with non-unity Lewis numbers.[4] Thus one can see that a model for the mean reaction can be obtained if a closure for the mean scalar dissipation rate is found. This fact has been recognized in many past studies and few models have been proposed for the mean scalar dissipation rate.[5–9]

In this spirit, Swaminathan and Bray[10] derived a transport equation for the mean scalar dissipation rate, which is exact when the Lewis number of reactant mixture is close to unity. A similar equation has also been obtained recently for non-unity Lewis number flames[11] and for the dissipation rates of intermediate species fluctuations.[12] This equation can be written as

$$\bar{\rho} \frac{D\tilde{\epsilon}_c}{Dt} - \frac{\partial}{\partial x_j} \left(\overline{\rho \alpha_c \frac{\partial \tilde{\epsilon}_c}{\partial x_j}} \right) + \underbrace{2\overline{\rho \alpha_c \alpha_c \left(\frac{\partial c''_{,k}}{\partial x_j} \frac{\partial c''_{,k}}{\partial x_j} \right)}}_{D_2} = T_1 + T_2 + T_3 + T_4. \tag{2}$$

The first, substantial derivative D/Dt, term represents temporal and convective changes of $\tilde{\epsilon}_c$ inside a control volume. The second term on the left-hand side represents diffusive flux while the third term signifies dissipation of the scalar dissipation rate. Out of the four terms on the right-hand side of Eq. (2), the first term, T_1, represents the turbulent transport and is given by[10]

$$T_1 \equiv \underbrace{-\frac{\partial \overline{\rho u''_j \epsilon_c}}{\partial x_j}}_{T_{11}} \underbrace{-2\overline{\rho \alpha_c u''_j \frac{\partial c''}{\partial x_k}} \frac{\partial}{\partial x_j} \frac{\partial \tilde{c}}{\partial x_k}}_{T_{12}},$$

where the Favre fluctuation of fluid velocity in direction j is denoted as u''_j. The influence of dilatation on the scalar dissipation rate denoted by T_2 is given as

$$T_2 \equiv 2\overline{\rho \epsilon_c \frac{\partial u_l}{\partial x_l}},$$

for unity Lewis number flames.[10] The interaction between turbulence and scalar gradient is given by[10]

$$T_3 \equiv \underbrace{-2\overline{\rho\alpha_c}\frac{\partial\tilde{c}}{\partial x_j}\left(\widetilde{\frac{\partial c''}{\partial x_k}\frac{\partial u_j''}{\partial x_k}}\right)}_{T_{31}} \underbrace{-2\overline{\rho\alpha_c}\left(\widetilde{\frac{\partial c''}{\partial x_j}e_{jk}''}\frac{\partial c''}{\partial x_k}\right)}_{T_{32}}$$
$$\underbrace{-2\overline{\rho\alpha_c}\left(\widetilde{\frac{\partial c''}{\partial x_j}\frac{\partial c''}{\partial x_k}}\right)\widetilde{e_{jk}}}_{T_{33}}. \quad (3)$$

The fourth term, T_4, representing contributions of chemical reactions is given by[10]

$$T_4 \equiv 2\left(\overline{\frac{\partial c''}{\partial x_k}\frac{\partial\dot{\omega}''}{\partial x_k}}\right).$$

In the above equations, the turbulent strain rate is denoted as $e_j'' = 0.5(\partial u_i''/\partial x_j + \partial u_j''/\partial x_i)$. Symbols t and x_j denote the time and the spatial position in direction j, respectively.

One way to obtain an algebraic model for the mean scalar dissipation rate, $\tilde{\varepsilon}_c$, is by balancing the leading order terms of Eq. (2) when the Damkohler number, Da, for the flame is large. This number is defined as the ratio of the large scale turbulence time scale to a chemical time scale and these two time scales are defined later. The leading order terms, identified using an order of magnitude analysis by Swaminathan and Bray,[10] are T_2, T_{32}, T_4, and D_2. All of these terms are unclosed and need to be modeled. The leading order nature of these terms and their modeling has been studied in the past using direct numerical simulation (DNS) data of statistically planar,[13–15] spherically symmetric,[16] and planar Bunsen[12] flames. The equation for the mean scalar dissipation rate transport and the correlation between velocity and scalar gradient in turbulent premixed flames have also been studied in detail by Mura *et al.*[17,18]

The reviews by Bilger *et al.*[19] and Driscoll[20] suggest that the mean reaction rate, thus the flame speed, is influenced by the turbulent flame geometries. Thus, one may expect some influence of flame geometry on the scalar dissipation rate and the various terms in Eq. (2). Indeed this has been shown[14,15] by comparing the behavior of these terms for statistically planar and spherical flames and the predominant influence was observed to be on the turbulent scalar interaction process represented by T_{32} in Eq. (3). This is because, the local dilatation created by the flame front strongly influences the mechanisms by which scalar gradients are produced. To shed more light on this, we briefly review the past works on this particular topic of turbulence-scalar interaction.

Recently, many studies have addressed this turbulence-scalar interaction process.[13,14,17,18,21–23] Swaminathan and Grout[13] first explained a fundamental difference in flame alignment with principal strain rates of turbulence in premixed flames. They showed that the scalar gradients have increased tendency to align with the most extensive component of the principal strain rate in turbulent premixed flames with high Da using DNS data. This tendency is in contrast to cold flow turbulence where scalar gradients tend to align with the most compressive principal strain rate. This difference is because of the strong influence of heat release rate on the dynamics of scalar mixing and this has also been confirmed in low Da turbulent premixed flames using data obtained from DNS of statistically one dimensional flames[13,14,16,21,24] and planar Bunsen flames.[12] This finding was also verified by Hartung *et al.*[22] using laser diagnostic data of bluff body stabilized turbulent premixed flames.

Our interest here is to study the interaction of turbulence and scalar field dynamics in statistically multidimensional turbulent premixed flames, specifically turbulent V-flames stabilized behind a cylindrical hot rod. This flame will have additional complexities due to mean flow divergence, mean shear produced because of wake behind the rod and its interaction with the flame, and competing effects of spatial decay of turbulence and its production via shear. The effects of mean shear on the turbulence scalar interaction can also be studied by comparing V-flame results to the insights obtained from statistically planar and freely propagating flames. The turbulence Reynolds number of these planar flames considered here are relatively large as will be noted later. Thus, the objectives of this investigation are (i) to conduct DNS of turbulent premixed V-flames in 3D with complex chemical kinetics and (ii) to gain further insight into turbulence-scalar interaction in premixed flames. This study involves hydrogen–air flames unlike earlier DNS studies, which considered hydrocarbon flame with either complex[12] or a simple one-step[12] chemical kinetics.

This paper is organized as follows. Detailed information about DNS of V-flames is discussed in Sec. II. The flame-brush structure along with the mean flow quantities are discussed in Sec. III A. The local conditions of turbulent combustion in the simulated flames are discussed in Sec. III B using a combustion regime diagram. The pdf of principal strain rates and their alignments with the flame normal are discussed in Sec. III C. The conclusions of this study are summarized in the final section.

II. DNS OF HYDROGEN-AIR TURBULENT PREMIXED FLAME

A. Governing equations

The governing equations are for the conservation of mass, momentum, energy, and species mass fractions. These equations can be written, respectively, as

$$\frac{\partial\rho}{\partial t} + \nabla\cdot(\rho\boldsymbol{u}) = 0, \quad (4)$$

$$\frac{\partial\rho\boldsymbol{u}}{\partial t} + \nabla\cdot(\rho\boldsymbol{u}\boldsymbol{u}) = -\nabla\cdot\boldsymbol{P}, \quad (5)$$

$$\frac{\partial\rho T}{\partial t} + \nabla\cdot(\rho\boldsymbol{u}T) = \frac{1}{\bar{c}_v}\nabla\cdot(\lambda\nabla T) - \frac{1}{\bar{c}_v}\sum_i(\rho Y_i\boldsymbol{V}_i c_{p,i}\cdot\nabla T)$$
$$-\frac{T}{\bar{c}_v}\sum_i R_i\nabla\cdot(\rho Y_i\boldsymbol{V}_i) - \frac{1}{\bar{c}_v}\boldsymbol{P}:(\nabla\boldsymbol{u})$$
$$-\frac{1}{\bar{c}_v}\sum_i(h_i w_i) + \frac{T}{\bar{c}_v}\sum_i(R_i w_i), \quad (6)$$

and

$$\frac{\partial Y_i}{\partial t} + \boldsymbol{u} \cdot \nabla Y_i = -\frac{1}{\rho}\nabla \cdot (\rho Y_i \boldsymbol{V}_i) + \frac{\omega_i}{\rho}, \tag{7}$$

where $\boldsymbol{u}$, T, and λ, respectively, denote fluid velocity vector, its absolute temperature and its thermal conductivity, respectively. The symbols Y_i, $\boldsymbol{V}_i$, R_i, h_i, and ω_i denote, respectively, mass fraction, diffusion velocity, characteristic gas constant, enthalpy, and reaction rate for species i. The specific heat capacities at constant volume and pressure for species i are denoted by $c_{v,i}$ and $c_{p,I}$, respectively. The stress tensor, $\boldsymbol{P}$, and the mixture averaged specific heat capacity at constant volume, $\bar{c}_v$, are, respectively, given by

$$\boldsymbol{P} = \left[p + \frac{2}{3}\mu(\nabla \cdot \boldsymbol{u})\right]\boldsymbol{I} - \mu\left[(\nabla \boldsymbol{u}) + (\nabla \boldsymbol{u})^T\right] \quad \text{and}$$
$$\bar{c}_v = \sum_i (c_{v,i} Y_i), \tag{8}$$

where μ denotes the dynamic viscosity of the fluid and $\boldsymbol{I}$ is the identity matrix. The thermodynamic pressure, p, is obtained using the state equation for multicomponent mixture, which is written as

$$p = \rho \mathcal{R} T \sum_i \left(\frac{Y_i}{W_i}\right), \tag{9}$$

where W_i denotes the molecular weight of species i and $\mathcal{R}$ is the universal gas constant.

The adiabatic combustion of stoichiometric hydrogen-air mixture at 0.1 MPa is simulated using a detailed kinetic mechanism,[25] which includes 27 elementary reactions and 12 reactive species (H_2, O_2, H_2O, O, H, OH, HO_2, H_2O_2, N_2, N, NO_2, and NO). The temperature dependence of the viscosity, thermal conductivity, and diffusion coefficients are calculated using CHEMKIN-II packages,[26,27] which are modified for vector/parallel computations. The effects of Soret, Dufour, and pressure gradient are neglected while calculating the diffusion velocity, $\boldsymbol{V}_i$, which is modelled using the Fickian type diffusion. The unburnt reactant temperature is set to 700 K for all the flames considered in this study. This preheating helps to reduce the stiffness in the set of equations given above for compressible reacting flows. These equations are discretized on a uniform spatial grid and are time advanced using third order Runge-Kutta scheme. The reaction terms are handled implicitly, using point implicit method. The spatial discretization schemes and boundary condition used depend on the flame configuration—either freely propagating planar or V flames considered in this study. These details are discussed in the following subsections.

B. Turbulent planar flame

The DNS of statistically planar turbulent flames is similar to the previous studies[28–30] from Tokyo-Tech and, here, we consider two planar flames, viz., P60 and P97. The turbulence Reynolds number, Re_λ, based on Taylor micro-scale for these flames are 60 and 97, respectively. The size of the computational domain for P60 is $10 \times 5 \times 5$ (in mm) and it is discretized using $513 \times 128 \times 128$ grid points. For the flame with higher Re_λ, the computational domain size is $14.8 \times 7.4 \times 7.4$ and the numerical resolution is $769 \times 256 \times 256$. These spatial resolutions give about 10 grid points inside the laminar flame thermal thickness in P60 and 15 grid points in P97 flames. Note that this resolution is based on the diagonal distance of a grid. The thermal thickness is defined as $\delta_L \equiv (T_b - T_u)/(|dT/d\zeta|_{\max})$, where T_b and T_u, respectively, denote the burnt and unburnt side temperatures and ζ denote the coordinate normal to the planar laminar flame. Also, these resolutions yield $k_{\max}\eta = 1.25$ for P60 and 1.16 for P97 flames, where $k_{\max}$ is the maximum wave number in each DNS case and η is the Kolmogorov length scale. The governing equations discussed in the previous subsection are discretized using fourth-order central difference scheme in x direction and by Fourier spectral method in the y and z directions. The finite difference scheme is used in the inhomogeneous direction, x, along which the flame-brush propagates. The homogeneous directions (y and z) are specified to be periodic and an inflow and outflow boundary conditions are specified for the x direction using NSCBC method.[31,32] The velocity field at the inflow boundary, $x = 0$, is specified to be $\boldsymbol{u}_{\mathrm{in}}(x = 0, y, z, t) = (\alpha S_L, 0, 0) + \boldsymbol{u}'_{\mathrm{in}}(y, z, t)$. The value of α, which is about the ratio of turbulent flame speed to laminar flame speed, is set to an optimal value for each case to avoid flame-boundary interaction at inflow or outflow boundaries. Here, $\alpha = 2.5$ and 3.0 for P60 and P97, respectively, and DNS is continued for long enough to construct statistically meaningful data. The turbulent velocity field $\boldsymbol{u}'_{\mathrm{in}}$ has been obtained in a preliminary DNS of homogeneous isotropic turbulence using spectral methods.[33] This fully developed turbulence field is fed from the inlet boundary of the computational domain for the reacting flow simulations, by interpolating this turbulence field onto a plane moving through this field at the mean velocity, $U_{\mathrm{av.}}$ This procedure is a standard practice in DNS of turbulent premixed flames. Typical iso-surfaces of normalized temperature, $c = (T - T_u)/(T_b - T_u)$, of 0.3 is shown in Figs. 1(a) and 1(b) for P60 and P97 flames, respectively. These iso-surfaces correspond to the location of maximum heat release and are shown at about 5.5 initial eddy turnover time, which is defined as $\tau_f = l_E/u_{\mathrm{rms}}$ using the turbulence integral length scale, l_E, and its rms velocity, u_{rms}, for the inflow turbulence. Figure 1 shows that the flame surface is distorted and contorted by the turbulence and the level of flame wrinkling is larger in P97 because of higher Re_λ. The fluid dynamic and thermochemical parameters describing the combustion conditions in these flames are given in Table I and it must be noted that these parameters are based on the characteristics of inlet turbulence. Here, S_L and δ_L denote the unstrained planar laminar flame speed and its thermal thickness, respectively. The Damköhler number is defined as $\mathrm{Da} = (l_E/\delta_L)/(u_{\mathrm{rms}}/S_L)$, and the Karlovitz number is defined as $\mathrm{Ka} = \delta_F^2/\eta^2$, where η is the Kolmogorov length scale and δ_F is the Zeldovich flame thickness defined as the ratio of kinematic viscosity, ν, to laminar flame speed, S_L. The values of Ka given in Table I are obtained using[10] $\mathrm{Ka} = \{[2(1+\tau)^{0.7}]^{-1}(u_{\mathrm{rms}}/S_L)^3(\delta_L/l_E)\}^{0.5}$. It is clear that the combustion conditions in the simulated flames are in the thin

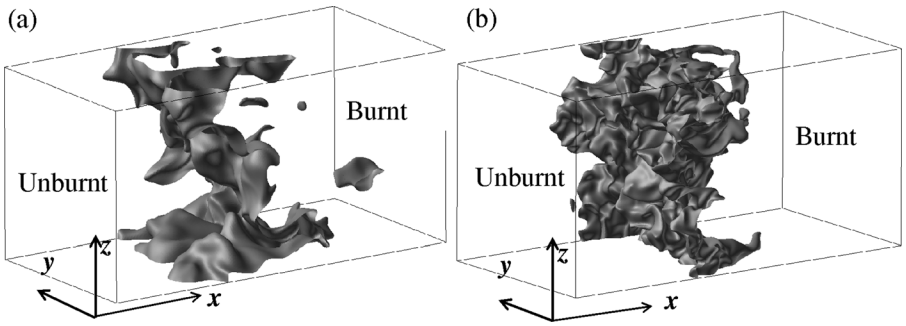

FIG. 1. Instantaneous iso-surface of the reaction progress variable, $c = 0.3$ in turbulent flame (a) P60 and (b) P97.

reaction zones regime. As one will note later, the combustion conditions remain in the thin reaction zones regime even if one uses the local Da and Ka.

C. Turbulent V-flame

Figure 2 shows a schematic of the turbulent V-flame simulated directly in this study and the turbulent flame is anchored using a hot rod of diameter $d \approx \delta_L$, which is located at a distance of about 2.5 to 5 mm from the inflow boundary. The temperature, velocity, and mass fraction of species inside the rod are fixed to be $T_{rod} = 2000\,\mathrm{K}$, $\boldsymbol{u}_{\mathrm{rod}} = 0$, and $Y_{i,\mathrm{rod}} = Y_{i,b}$, respectively. Here, $Y_{i,b}$ denotes the mass fraction of species i in fully burnt mixture. Before the simulations are begun, these values are smoothly matched to the free stream values using a Gaussian function given by

$$\mathcal{G}(r, t=0) = (\mathcal{G}_{\mathrm{rod}} - \mathcal{G}_{\infty}) \exp\left[\frac{(r - r_w)^2}{2r_w^2}\right] + \mathcal{G}_{\infty}, \qquad (10)$$

where $\mathcal{G}$ denotes either fluid velocity components or temperature or species mass fractions, r is the radial distance from the rod center, $r_w = d/2$ is the radius of the rod and the subscript ∞ denotes the free stream value, which is the value specified at the inflow boundary. The fluid velocity, $\boldsymbol{u}$, at the inlet boundary is specified to be a sum of an average velocity, $\boldsymbol{U}_{\mathrm{av}}$, and a turbulent fluctuation, $\boldsymbol{u}'_{\mathrm{in}}$. The average velocity is taken to be $\boldsymbol{U}_{\mathrm{av}} = (U_{\mathrm{av}}, 0, 0)$ and the turbulent velocity fluctuations are obtained from *a priori* simulations of incompressible turbulence as has been done for the planar flames. After this initialization, the simulations were run for 3 flow-through time, $\tau_D = L_x/U_{\mathrm{av}}$, where L_x is the computational domain length in the direction x noted in Fig. 2.

Three V-flames are computed for the conditions given in Table I. The mean inflow velocity for V60H flame is twice larger than for V60 and both of these flames have the same turbulence level at the inflow boundary. The flame V97 has

TABLE I. Combustion conditions of planar and V flames based on inflow turbulence characteristics.

	Case	Re_λ	U_{av}/S_L	u_{rms}/S_L	l_E/δ_L	Da	Ka
Planar	P60	60.8	2.5	2.2	1.6	0.73	1.3
	P97	97.1	3.0	4.1	2.2	0.52	2.8
V-flame	V60	60.8	10	2.2	1.6	0.73	1.3
	V60H	60.8	20	2.2	1.6	0.73	1.3
	V97	97.1	20	6.0	1.5	0.24	6.2

$U_{\mathrm{av}} = 20\,S_L$ and $u_{\mathrm{rms}} \approx 6\,S_L$. The computational domain size, $L_x \times L_y \times L_z$, for these flames are $10 \times 5 \times 5$ (in mm) for V60 and V97, and $12.5 \times 5 \times 5$ for V60H. The governing equations presented in Sec. II A are discretized inside these computational domains using a fourth-order central difference scheme. The uniform numerical grids used are $513 \times 257 \times 257$ for V60, $641 \times 257 \times 257$ for V60H and $769 \times 385 \times 385$ for V97, which insures that there are at least 20 grid points inside δ_L in each case. Also, this grid resolution is more than sufficient to resolve the boundary layers near the rod, which has been verified by studying simulation results for the spatial variation of instantaneous velocities, temperature, and mass fractions in neighborhood of the rod. Furthermore, the length scales of progress variable, l_c, and its Favre fluctuation, $l_{c''}$, are estimated using $l_c = 1/|\nabla c|_{\max}$ and $l_{c''} = 1/|\nabla c''|_{\max}$ and compared with a resolution vector length of a grid, $dl = (dx^2 + dy^2 + dz^2)^{0.5}$. The ratios between each of these length scale and the resolution vector length, l_c/dl and $l_{c''}/dl$, vary in the range of about 4.3 to 7.2, which suggests that the spatial resolution is adequate to resolve scalar gradients. The location of the rod from the inlet boundary in V60H case is twice farther compared to V60 case in order to maintain the turbulence level just ahead of the rod in these two cases. The DNS results shown in Fig. 3 support this and this specific condition is

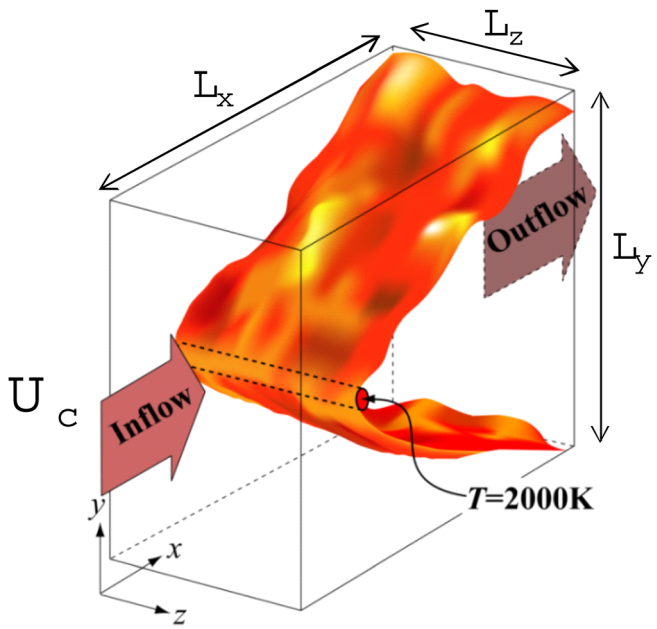

FIG. 2. (Color online) Computational configuration used in turbulent V-flame simulations.

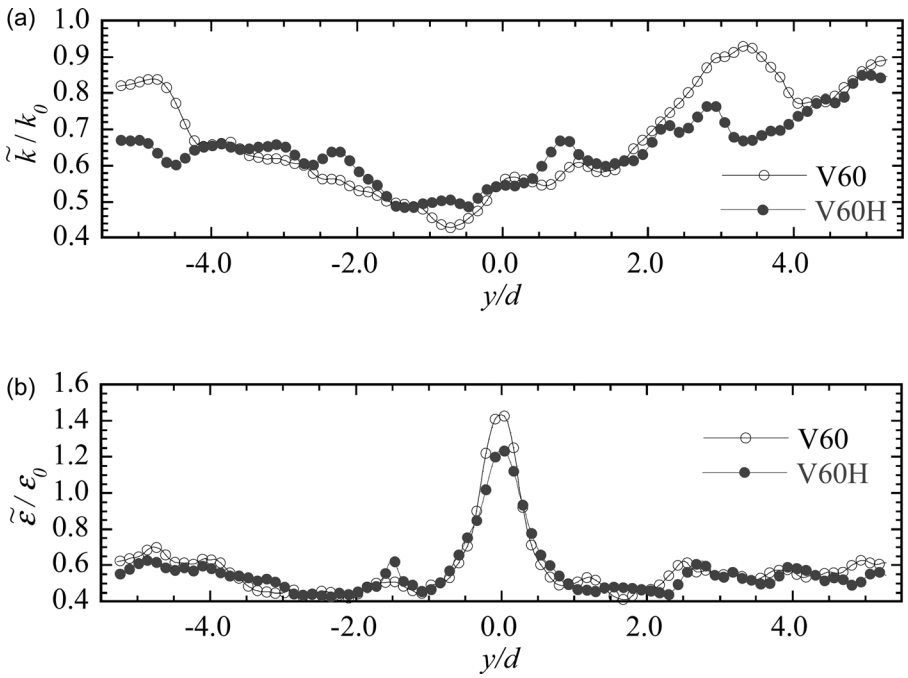

FIG. 3. (a) and (b) Cross stream variation of turbulent kinetic energy and its dissipation rate at location $1.2d$ upstream of the rod from cases V60 and V60H.

chosen so that the observed differences, to be discussed later in Sec. III, between cases V60 and V60H are predominantly due to the difference in U_{av} and are not compounded by the effects of change in turbulence. The computational boundaries in the inhomogeneous directions x and y are specified appropriately to be inflow or outflow boundaries using NSCBC methods[31,32] and a periodic boundary condition is used for the homogeneous direction z.

D. Data processing

Figure 4 shows the Favre averaged progress variable, $\tilde{c}$, contours along with sampling volumes shown as the colored boxes used to construct various statistical quantities of interest for this study. Detailed discussion on the mean progress variable is given later. The size of the sampling volume is $5 \times 5 \times N_z$, where N_z is the number of grid points used in the homogeneous direction, z. The sampling volumes are taken from five streamwise locations and these locations are $x_1 = d$, $x_2 = 2d$, $x_3 = 5d$, $x_4 = 9d$, and $x_5 = 14d$, where d is the diameter of the rod. The mean value of a quantity, say Q, is obtained by averaging in a sample volume at (x_0, y_0) as well as over sampling period using

$$\bar{Q}(x_0, y_0) = \frac{1}{25 N_t N_z} \sum_{n=1}^{N_t} \sum_{k=1}^{N_z} Q(x_0, y_0; k, n), \qquad (11)$$

where $N_t = 6$ is the number of data sets collected from the computational volume over the last two flows through time after allowing the initial transients to exit the domain. The fluctuating quantity, $q'(x, y, z, t)$ is then obtained by subtracting $\bar{Q}$ from $Q(x, y, z, t)$. The spatial variation of $\bar{Q}$ is obtained by moving this sample volume across x and y as shown in Fig. 4. For the planar flames, the averaging direction also includes y direction, since it is also homogeneous. Equation (11) is also used after weighting it with density appropriately to obtain Favre averages.

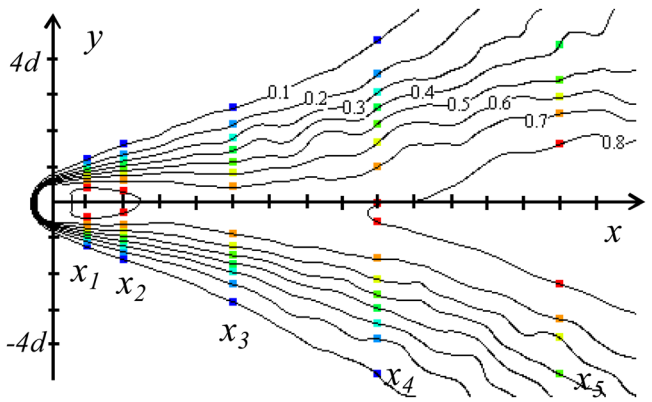

FIG. 4. (Color online) Location of sampling volumes used to construct various statistics discussed in this paper. The contours are time and spatially (in the homogeneous direction) averaged reaction progress variable from simulation V60.

III. RESULTS AND DISCUSSION

A. General characteristics

Fluid dynamics in turbulent V-flames consist on the balance between decays of turbulence and the production of turbulence due to the mean shear or the wake as well. The wake region behind the rod spreads by turbulent diffusion and the flame-brush is contained within the shear dominated region of the wake as one shall see later (cf. Figs. 4, 5(a), and 11). Although this is well known from a number of experiments, the interplay among heat release, turbulence, shear, and their influences on the turbulence-chemistry interaction is not fully understood. As noted in the Introduction, the aim of

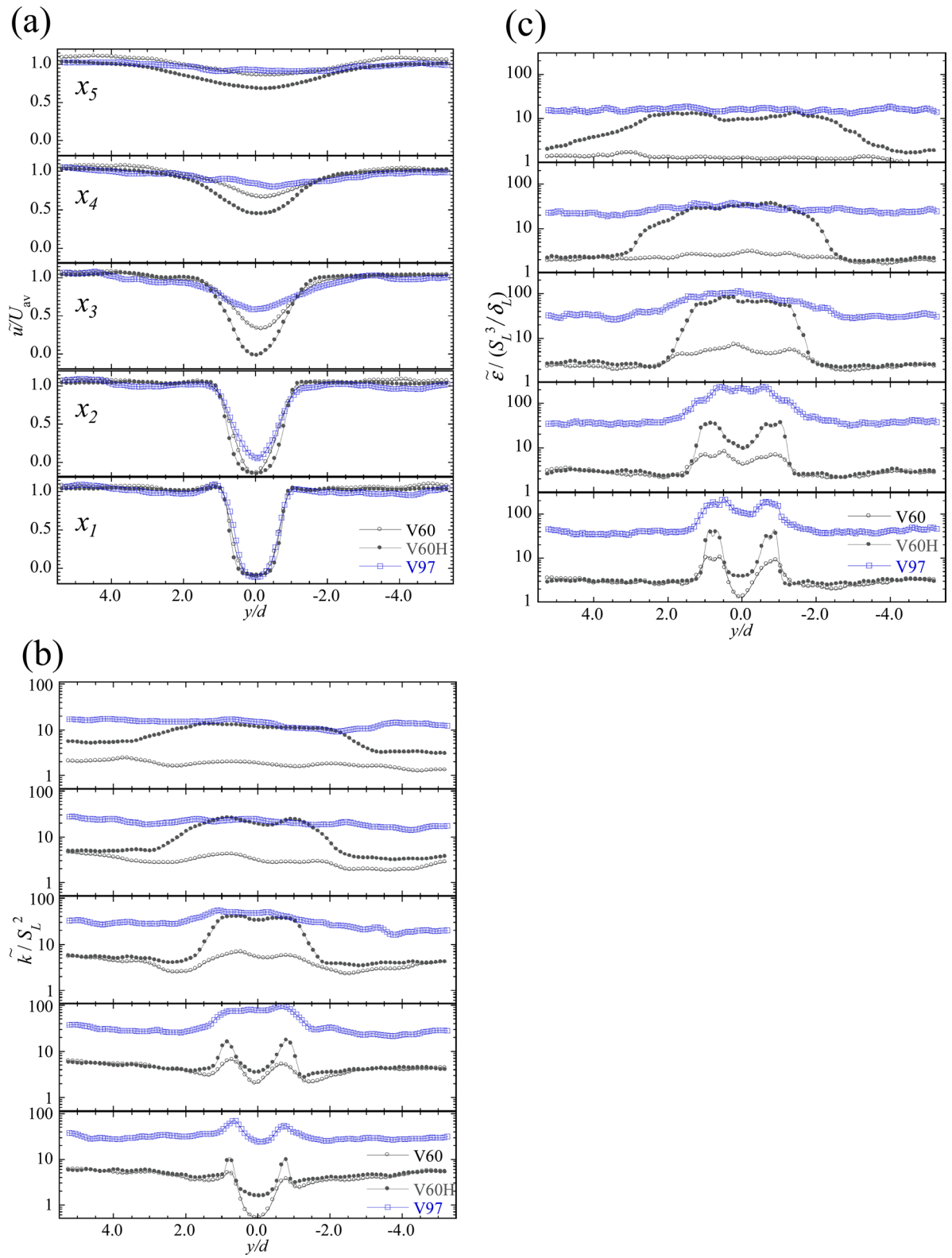

FIG. 5. (Color online) (a)–(c) Variation of normalized Favre mean (a) velocity, (b) turbulent kinetic energy, and (c) its dissipation rate, with y/d in three V-flames simulated; open circle: V60, filled circle: V60H, and square: V97. The results are shown for five streamwise positions marked in Fig. 4.

this investigation is to analyze the DNS data to study turbulence-scalar interaction in the presence of mean shear which is produced by the flow and flame. Before analyzing flame related quantities, the turbulence characteristics in the simulated V-flames are studied first.

1. Flow and turbulence characteristics

The cross stream variations of the Favre averaged mean velocity, turbulent kinetic energy, and its dissipation rate are, respectively, shown in Figs. 5(a)–5(c) for five streamwise

locations. The Favre mean velocity is normalized using the incoming average velocity, $U_{\text{av,}}$ and the turbulent kinetic energy and its dissipation rate are normalized appropriately using the planar laminar flame speed and its thermal thickness. The results are shown for all three V-flames simulated. The variation of mean velocity is as expected and it shows a negative velocity in the near field (up to x_2) because of the presence of the recirculation zones behind the rod. The variation of $\tilde{u}/U_{\text{av}}$ at x_3 location suggests that the length of the recirculation region is about $5d$ in V60H case and it is about $2d$ in V97 case. These two flames have the same $U_{\text{av}} = 20\,S_L$ and different u_{rms} for the incoming stream as given in Table I. The turbulence level in V97 case is nearly three times larger than in V60H case and the reduced size of the recirculation zone in the V97 case is because, the higher turbulence level enhances the momentum exchange behind the rod. The results in Fig. 5(a) clearly suggest that V60H case has longer recirculation zone than V60 case due to higher mean velocity, $U_{\text{av.}}$ It is worth to note that the distance between the rod center and the inlet boundary in the case of V60H is twice the value in V60 case as noted earlier. This ensures that the turbulent kinetic energy and its dissipation rate at a location just ahead of the rod in V60H case is almost the same as in V60 case (see Fig. 3) suggesting that the observed difference between V60 and V60H cases is mainly due to changes in $U_{\text{av.}}$ A close study of Fig. 5(a) shows that $\tilde{u}/U_{\text{av}} > 1$ for $|y|/d > 3$ in the near filed and this overshoot disappears as one moves in the downstream direction. The overshoot in the near field occurs to conserve the mass and also at about $y/d \approx 1$ for x_1 there is a strong spatial acceleration because of heat release effects.

The variations of normalized turbulent kinetic energy and its dissipation rate are shown in Figs. 5(b) and 5(c), respectively. Note that a logarithmic scale is used for the ordinate of these two figures. The behavior of these two quantities is very similar. The shear production of turbulent kinetic energy, denoted by the two peaks, is obvious in these figures. These two peaks move towards each other with downstream distance because of turbulent diffusion and merges together. This merging yields a plateau in the central region and it occurs quicker in V97 because of increased level of turbulence in the incoming stream in addition to shear production. The relatively larger peaks in V60H compared to V60 is because of higher shear produced by larger $U_{\text{av.}}$ The spatial decay of the incoming turbulence is also seen in the outer region, $|y|/d \geq 4$. The variation of normalized dissipation rate shown in Fig. 5(c) is consistent with the variation of turbulent kinetic energy.

The ratio of mean and turbulent strain rates, $\mathcal{R} = \sqrt{\tilde{e}_{ij}\tilde{e}_{ij}/e''_{ij}e''_{ij}}$, is shown in Fig. 6 for V60H flame at five streamwise locations as a function of y/d. The peak at $y/d = 0$ for x_1 is because of the recirculation zone behind the rod. It is clear that the mean shear is large inside the shear layers where the combustion occurs. At locations x_1 and x_2, the mean shear is dominant. The ratio, $\mathcal{R}$, decreases with the streamwise distance from the rod, and the effect of mean shear becomes small compared to the turbulence strain for $x \geq x_4$. This variation for V60 and V97 cases (not shown) is similar to that shown in Fig. 6. The peak value of $\mathcal{R}$ for V60 case is about 2, and 0.95 for V97, whereas it is larger than 3 for V60H (see Fig. 6). From the downstream location x_3 onwards, the value of $\mathcal{R}$ varies around 0.5 as in Fig. 6 for all these flames.

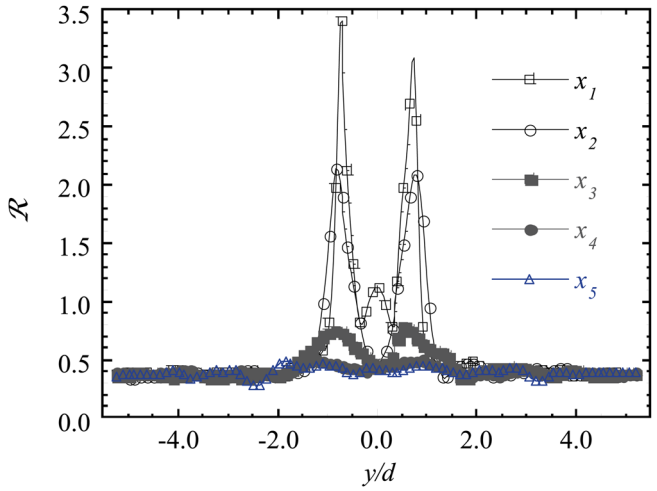

FIG. 6. (Color online) Variation of the ratio between mean and turbulent strain rates for V60H.

2. Flame structure

Since the flame structure in the progress variable space does not depend on the flame configuration, here, we use the progress variable space to study the flame front structure. The progress variable can be defined using temperature, T, or fuel mass fraction, Y_{H_2}, or the mass fraction of water vapor, $Y_{\text{H}_2\text{O.}}$ These three progress variables are, respectively, defined as $c = (T - T_u)/(T_b - T_u)$, $c_{\text{H}_2} = 1 - Y_{\text{H}_2}/Y_{\text{H}_{2,\text{u}}}$, and $c_{\text{H}_2\text{O}} = Y_{\text{H}_2\text{O}}/Y_{\text{H}_2\text{O,b}}$, where the subscripts u and b denote the unburnt and burnt gases, respectively. The scatter plots shown in Fig. 7 depict that the effects of non-unity Lewis number, the complex kinetics and temperature dependent transport coefficients used in the simulations. The data is randomly sampled, 1 in every 20 points are shown, at locations x_2 and x_4 in the V97 flame. Since both H_2 and H_2O are mobile with $Le \sim 0.3$ and $Le \sim 0.8$, the progress variables show larger value than c. The difference of variations between $c - c_{\text{H}_2}$ and $c - c_{\text{H}_2\text{O}}$ comes from the use of complex chemistry in which the temperature rise and the consumption/production of species are not correlated linearly. If these three definitions are equivalent then one would see that the data points would fall along the diagonal lines shown. The instantaneous progress variables show that the influences of non-unity Lewis number prevail in the flame V97 with the highest turbulence considered here. Their average values shown in Fig. 8 clearly suggest that the non-unity Lewis number effects are not influenced by the turbulence Reynolds number, at least for the range considered here. However, the progress variable based on T is chosen for further analysis as the results reported here are not unduly influenced by this choice.

Typical variation of temperature in the local normal direction is shown in Figs. 9(a) and 9(b) for the three V-flames simulated. The distance in the local normal

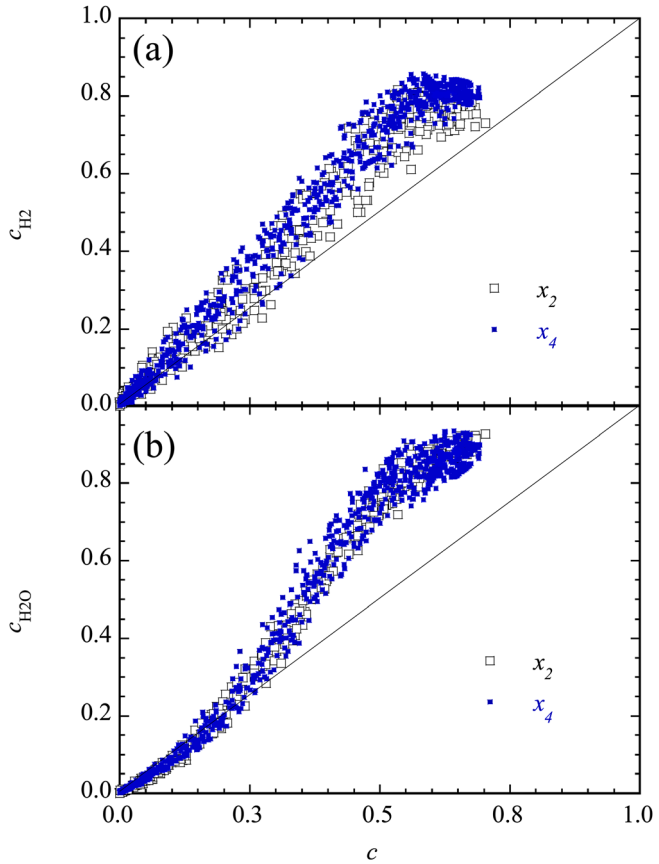

FIG. 7. (Color online) Scatter plot of (a) c vs c_{H_2} and (b) c vs c_{H_2O} from simulation V97 at locations x_2, x_4 for an arbitrary instant.

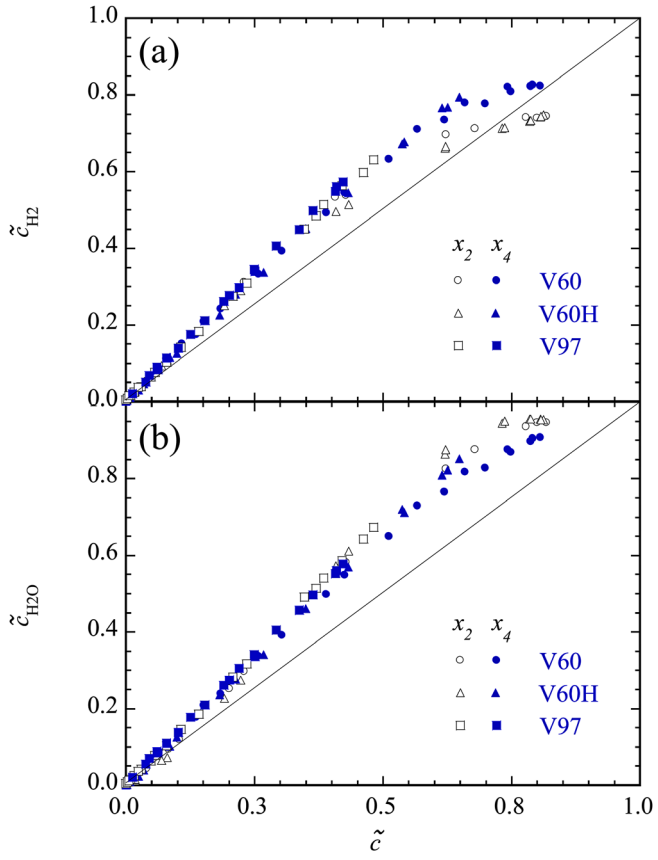

FIG. 8. (Color online) Scatter plot of (a) $\tilde{c}$ vs c_{H_2} and (b) $\tilde{c}$ vs c_{H_2O} from simulation V60, V60H, and V97 at locations x_2 and x_4.

direction, n, is normalized using the planar laminar flame thermal thickness and $n=0$ in these plots corresponds to the position of peak heat release rate. The local normal is defined based on the progress variable gradient, ∇c, at the location of peak heat release rate for a given (x,z) position. The bold solid circle is the data for unstrained planar laminar flame computed using the same chemical kinetics and thermochemical conditions as that of the DNS. The lines with symbols are for the three V-flames for streamwise locations, x_2 and x_4, noted in the figure and they represent averaged, both in time and homogeneous direction (see Eq. (11)), values. The small symbols (scattered) represent instantaneous temperature taken at various positions taken along the homogeneous direction for V60 flame. The scatter shown in these two figures are typical for V60 and V60H flames and the fluctuation is observed to be some what larger for the V97 case (not shown) when $n/\delta_L > 0.5$. This larger fluctuation on the burnt side gives a lower mean temperature in V97 case compared to the laminar flame as shown in Figs. 9(a) and 9(b). Also the interaction of flame-brushes, as one shall see in Fig. 11 later for V97 case, as well as the interaction of flamelets in Fig. 10, leads to lower temperature on the burnt side. The instantaneous temperature field in $z=0.3l_z$ and $0.8l_z$ planes is shown for V97 case in Fig. 10 with the sampling locations, x_2 and x_4 marked. At locations x_2 (a) and x_4 (b), due to the flame interaction, it is clear that the variation of progress variable along the flame normal direction does not increase with the normal distance. Such interactions appear in V97 case in other locations at different time as well, due to the high turbulence intensity, and this interaction is not negligible even in an average sense as one shall see the temperature drop on the burnt side shown in Fig. 9 and the interaction of flame-brushes shown in Fig. 11.

Although the scatter in Fig. 9(a) suggests that the flame front may not be flamelet like at location x_2 for the V60 case, the averaged temperature variation suggests a flamelet like combustion, although $Da<1$ for the V60 flame as noted in Table I. However, as one shall see in Sec. III B, local combustion conditions in this flame are in the border between the corrugated flamelets and the thin reaction zones regimes. A similar observation is made for the planar flames P60 and P97 (not shown here) and the local combustion conditions in the flame P97 are in the thin reaction zones regime. These observations are consistent with a recent numerical study[34] of stoichiometric hydrogen-air combustion in the distributed reaction zones regime, with $Da \approx 0.1$, $u_{rms}/S_L \approx 35$ and $l_E/\delta_L \approx 2$, and an experimental investigation[35] of CNG-air flames with Da ranging from 0.005 to 0.07. It is also worth noting that the DNS for this study used a multi-step chemical kinetics while a single step irreversible reaction is used by Poludnenko and Oran.[34]

A close study of Fig. 9(a) shows some deviation of the averaged temperature from the laminar flame values even for the V60 case when $n/\delta_L > 0.5$. This deviation decreases as one moves downstream, see the result shown in Fig. 9(b) for x_4 location. Also, Fig. 9(a) shows that the averaged

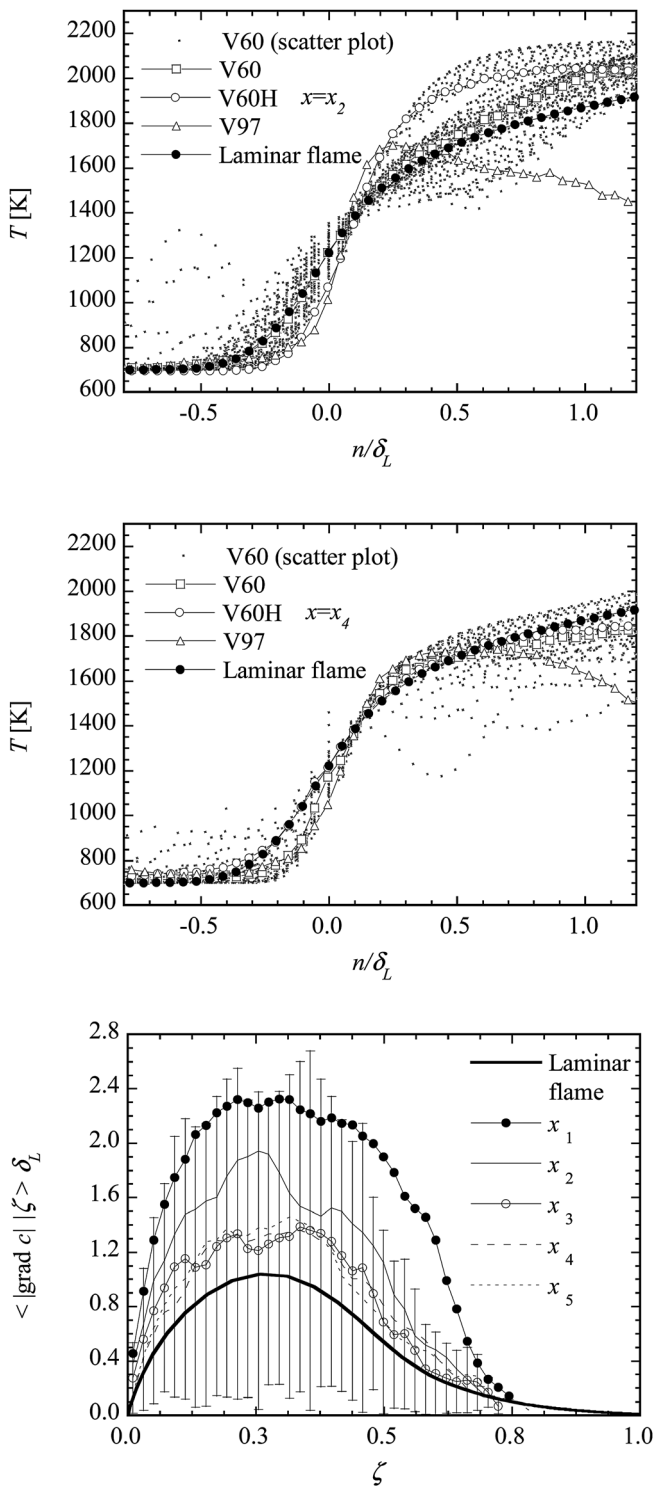

FIG. 9. (a)–(c) Comparison of temperature variation along the local flame normal in V-flames and planar laminar flame at locations x_2 in (a) and x_4 in (b). The variation of conditionally averaged $|\nabla c|$, normalized using the planar laminar flame thermal thickness, in V97 flame is compared to the laminar flame results in (c) for few downstream locations.

temperature variation in the V60H and V97 flames for location x_2 deviates from the unstrained planar laminar flame values, which suggest thinner flame fronts in these turbulent flames. This strain thinning is not because of turbulent strain, since the flame fronts in V60 and V60H cases experience a similar level of turbulence on an average (see Table I and Fig. 3), but due to the effects of mean strain, which is twice larger in V60H compared to V60. However, the influence of mean strain seems to weaken as one moves downstream and the structure of unstrained planar laminar flame is recovered as the flamelet structure. This is also verified by computing the average of progress variable gradient magnitude, $\langle|\nabla c||\zeta\rangle$, conditional on a value of the progress variable $c=\zeta$. This result is shown in Fig. 9(c) for the V97 case and the conditional average is normalized by the laminar flame thermal thickness, δ_L. The normalized conditional average is shown for five streamwise positions for the sampling volume located at $\tilde{c}=0.2$ (see Fig. 4). The vertical bar shows the range, maximum, and minimum, of the conditional average observed for a given value of ζ at location x_3. There are minimum of about 1300 samples for the data points shown in Fig. 9(c). Since no samples are observed for $\zeta>0.8$, the curves in Fig. 9(c) for the turbulent flame end abruptly. The unstrained planar laminar flame result is also shown depicting a smooth variation for large ξ values with a peak value near $\xi=0.3$. This is because, the chemical activation occurs at lower temperature for stoichiometric hydrogen-air flame.[36,37] The peak value in the laminar case is 1 and it increases by about 60% in V60 flame for location x_1, but in V60H this peak value increases to 2.2. One can observe that this value is only about 2.3 in V97, despite u_{rms} is increased to 6.0. It is clear that the strong mean strain at locations just downstream of the rod thins the flame front leading to larger gradient. The conditional average slowly moves towards the planar laminar flame values at downstream locations suggesting the recovery of unstrained planar laminar flame structure eventually as noted earlier. However, for the flames studied here, the laminar flame value for $|\nabla c|$ are not reached in the computational domain, since the turbulence experienced by the flamelets at the downstream locations is still substantial as shown by $\tilde{k}$ values in Fig. 5(b). These behaviors are not noted for the planar flames, P60 and P97, and the conditional progress variable gradient is observed to remain close to the planar laminar flame values almost at all locations inside the flame-brush.

Spatial variations of the Favre mean progress variable, $\tilde{c}$, and its variance, $\widetilde{c''^2}$, are shown in Fig. 11 for the three V-flames. The grey scale for the top row represents $\tilde{c}$, and $\widetilde{c''^2}$ for the bottom row. The contour lines are the mean reaction rate, $\bar{\dot{\omega}}$, of the progress variable normalized using $\rho_u S_L/\delta_L$. The lack of symmetry in the structure of the flame-brush about the x axis shown in Fig. 11 is because of limited sample size available for averaging. The effect of mean flow velocity on the flame-brush can be seen clearly by comparing the figures in the top row. As noted in many earlier experiments,[38–40] the mean flame angle is reduced by the increase in the mean velocity. The Favre variance is seen to be large in regions with high turbulence level and reaction rates, since this variance is produced by the effects of mean scalar gradient and chemical reactions. In the V60 and V60H cases, one may note a reasonably good correlation between the variance and the mean reaction rate as noted in many premixed combustion models,[7,41,42] and the predominant combustion is seen to occur in the mixing or shear region behind the rod. For V97 flame, the mean reaction rate seems to be

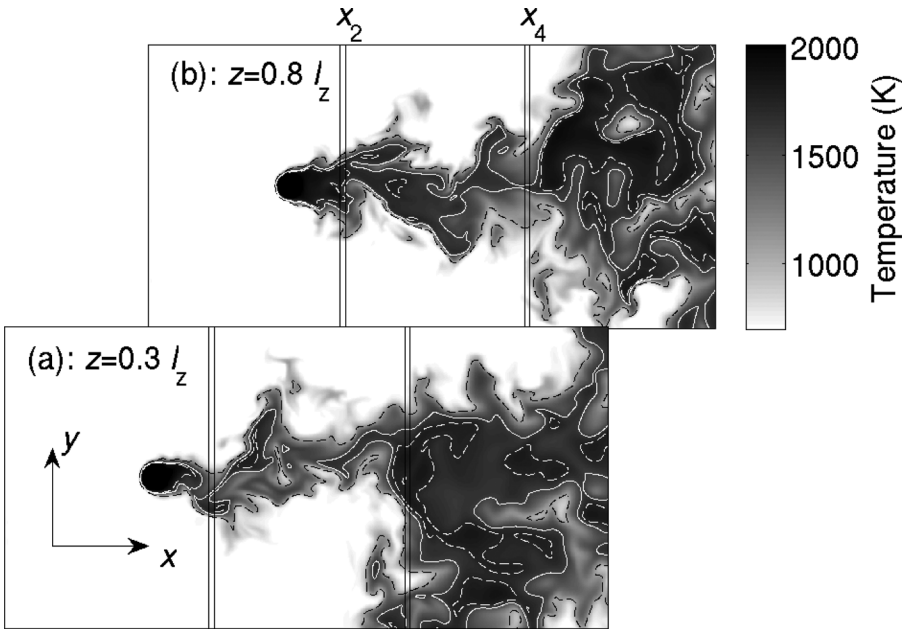

FIG. 10. Instantaneous temperature field as two-dimensional slice for V97 case. Black solid lines show the sampling locations, x_2 and x_4. Black dashed lines: 1100 K, white solid lines: 1600 K, and white dashed lines: 1750 K.

uncorrelated with $\tilde{c}$ and $\widetilde{c''^2}$. This is due to the contribution of turbulence strain to the mean reaction rate ($\tilde{\epsilon}/\tilde{k}$, see Figs. 5(b) and 5(c) at location x_5). There is no combustion (mean reaction rate) in the center of the wake in the V60 flame and there is some combustion in V60H case. However, combustion in the center of the wake region is noted to be substantial in the V97 case. Although the mean velocity is the same in V60H and V97 flames, the higher level of turbulence in V97 increases the mean flame angle because of turbulent diffusion. The mean reaction rate contours show that the reaction zones are shredded in V97 case. Also, a close investigation of Fig. 11 clearly shows that the intense reaction zones with $\bar{\dot{\omega}} > 0.5\rho_u S_L/\delta_L$ are elongated in V60H case because of larger $U_{\text{av,}}$ however an increase in u_{rms}/S_L in the V97 case decreases the length of this reaction zone. This is because of the increase in the turbulent transports, which creates a wider flame brush and shorter recirculation zone behind the rod. This is apparent in the V97 case shown in Fig. 11.

The variation of turbulent flame-brush thickness normalized using the planar laminar flame thermal thickness with x/d is shown in Fig. 12 for the three V-flames. The flame-brush thickness is obtained as $\delta_t = (|\partial\tilde{c}/\partial y|_{\max})^{-1}$ for every streamwise position. Two values of δ_t for a given x is because of the two flame-brushes, top and bottom, shown in Fig. 11. This quantity has been studied in many earlier experimental studies and the results are summarized by Lipatnikov and Chomiak[43] (see their Fig. 7). These studies have shown an increase in the flame-brush thickness with time normalized by turbulent eddy turnover time, τ_f, and this is somewhat different from the results shown in Fig. 12. Also, Lipatnikov and Chomiak[43] showed that the evolution of the flame-brush thickness is well predicted by Taylor's theory of turbulent diffusion for a passive scalar.[44] This theory predicts a linear growth in t for the rms displacement of a fluctuating passive scalar iso-surface when $t \ll \tau_f$ and this growth becomes $\sqrt{t}$ when $t \gg \tau_f$. This displacement thickness is

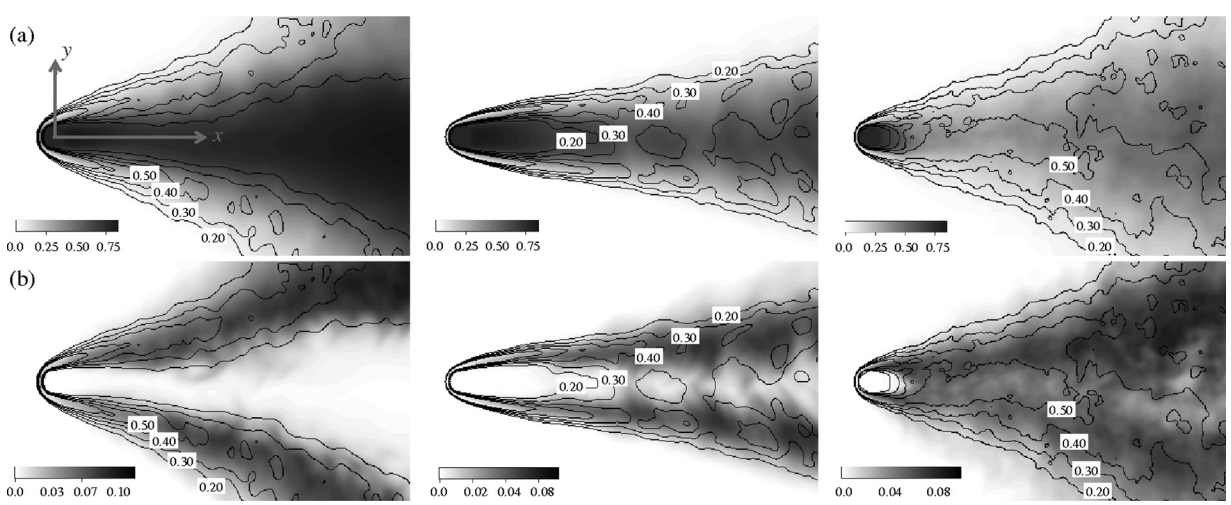

FIG. 11. Spatial variation of (a) $\tilde{c}$ and (b) $\widetilde{c''^2}$ in the three V-flames are shown in gray scale and the black contours represent the mean reaction rate of the progress variable normalized appropriately using the unstrained planar laminar quantities, ρ_u, S_L, and δ_L.

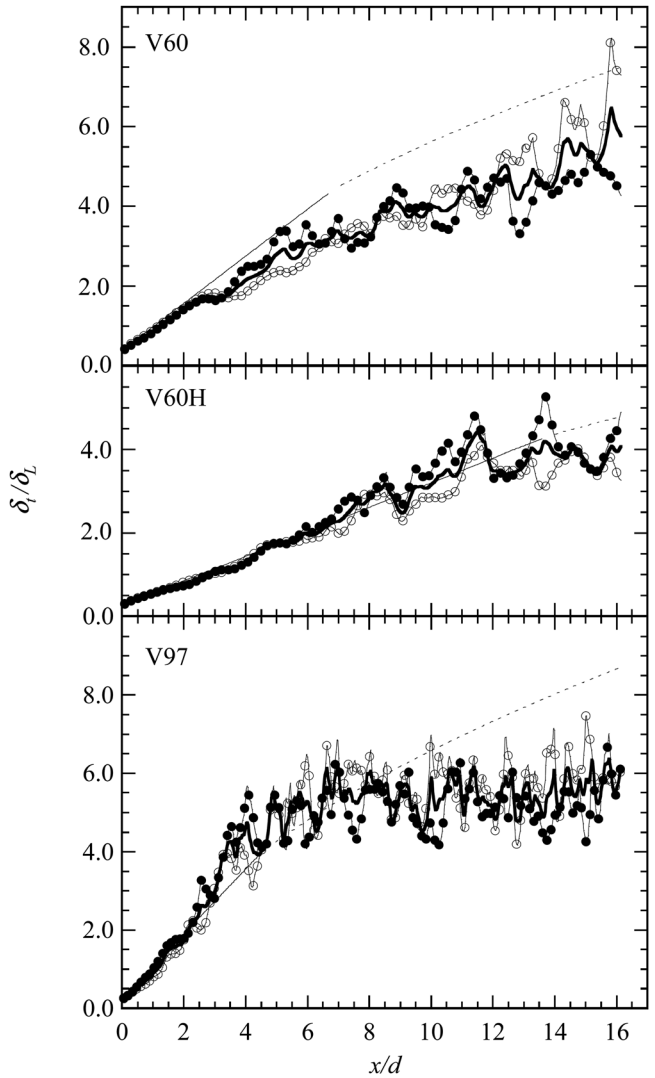

FIG. 12. Variation of flame-brush thickness with streamwise distance, normalized by the rod diameter d, in V60, V60H, and V97 flames. The flame-brush thickness is normalized by the thermal thickness. Lines with symbols are for the two wings of the V-flames, thick solid line represents the average value. The thin lines are from Taylor's theory of turbulent diffusion.[44]

noted to represent the turbulent flame-brush thickness, δ_t, by Lipatnikov and Chomiak (see their Eqs. (4) and (5)) and it is verified in Fig. 12. If one can translate t/τ_f to x/d by using the Taylor hypothesis then $t/\tau_f \simeq 1$ is equivalent to $x/d = 7.2$ for V60, 15 for V60H and 5 for V97 flames after using the parameters given in Table I. The linear variation is shown as a thin solid line and dashed line represents the square root dependence. A gap in the theoretical curve is intentionally made to mark some transition from linear to square root regime. It is clear that the turbulent diffusion theory of Taylor works well for V60 and V60H, except for a constant of proportionality in V60 flame. The turbulence level is small for these two flames, and the flame-brushes remain spatially separated and do not interact with one another as shown in Fig. 11. The spatial separation of the flame-brushes is clear in the images containing Favre variance. Although the linear regime is predicted well even for the V97 case, the flame-brush thickness is seen to saturate at about 5.5 δ_L for $x > 7d$. This behavior could be because of the interacting flame brushes as shown in Fig. 11, which also depicts the mean reaction rate contours shredded by the turbulence.

The flame-brush thickness seems to grow with x/d for the flames V60 and V60H having low turbulence level. However, for the V97 case, the flame-brush thickness is seen to level off after $x/d \approx 6$, which agrees with the above estimate reasonably well. This seems to suggest a balance between the turbulent diffusion, which increases the flame brush thickness, and the chemical reaction, which is expected to increase the gradient, for $x/d > 7$. It has been shown in other studies[45,46] that the growth of δ_t is represented well by Taylor's theory[44] of turbulent diffusion and the results shown here in Fig. 12 also agrees with this when there is no interacting flame brushes. From a practical point of view, one must consider this interaction because practical flames are usually constrained in space.

B. Combustion regimes

It is a general practice to use turbulence characteristics at the inlet to designate combustion conditions in turbulent premixed combustion studies. Indeed, the combustion condition or regime will be determined by local turbulence and thermochemical conditions and these attributes are influenced by a number of factors such as shear, flow entrainment, turbulence decay, etc. The numerical flames considered in this study include turbulence decay and mean shear effects and, thus, the local combustion conditions are studied using a combustion regime diagram[41] as shown in Fig. 13. Gray, blue, and orange small squares in this figure show the local combustion conditions, respectively, in the V60, V60H, and V97 flames. The data is randomly sampled (one in every 25 points) inside the flame-brush over the entire domain and covers a wide range of combustion conditions. Almost all of the data is in the thin reaction zones regime with $Da_L < 1$ with a small fraction crossing the $Da = 1$ line. The samples below the $Re = 1$ line come from the region just behind the rod (x_1 and x_2 in Fig. 4). If one averages these scatter plots at given x locations, the averaged condition moves from left-top to right-bottom as the downstream distance increases. The white circles, triangles, and

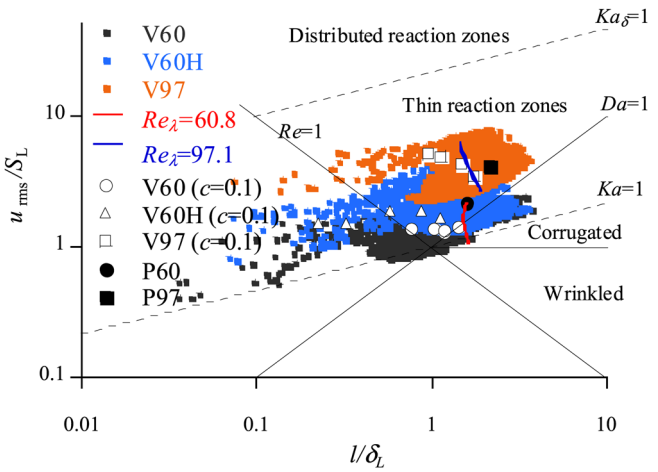

FIG. 13. (Color online) Combustion regime of the present DNS on the turbulent combustion diagram.

squares are obtained by using turbulence conditions in sampling volumes shown in Fig. 4 along $\tilde{c} = 0.1$ contour line and one moves from left to right along these symbols as the downstream distance behind the rod increases. This implies that the local Damkohler number increases, slowly compared to the two solid lines, as one moves downstream supporting the recovery of flamelet structure shown in Fig. 9. The thick solids lines are constructed using turbulence characteristics, which are not influenced by the mean shear or combustion. These characteristics are obtained by running a homogeneous isotropic turbulence decaying from the initial conditions used for the planar and V-flame simulations. This comparison is shown to bring out the influence of mean shear on the local combustion conditions. The solid black circle and square, respectively, represent combustion conditions in P60 and P97 flames based on the turbulence characteristics at the inflow boundary (see Table I). If one uses the inflow turbulence characteristics for V60 and V60H then the black solid circle would represent the combustion conditions of these two flames as noted in Table I. However, one can clearly see that this is only one point in the spread shown in Fig. 13 for V60 and V60H flames. Any reasonable combustion model, either RANS or LES, must be able to respond to these local changes in combustion conditions.

C. Turbulence-flame interaction

As noted earlier in Sec. I, the main aim of this work is to investigate the effects of flame geometry and also Da on turbulence-scalar interaction process represented by T_{32} in Eq. (3). The effect of Da is addressed in an earlier study using statistically one dimensional and planar flame data.[14,47] Here, statistically multidimensional flames are considered. The T_{32} term can be written as

$$T_{32} = -2\rho\alpha_c\overline{|\nabla c''|^2(\alpha\cos^2\theta_\alpha + \beta\cos^2\theta_\beta + \gamma\cos^2\theta_\gamma)}, \quad (12)$$

using eigenvalue decomposition. The symbols α, β, and γ are eigenvalues of turbulent strain tensor, e''_{jk}, which are ranked as $\alpha > \beta > \gamma$, where α is the most extensive principal strain rate, β is the intermediate principal strain rate, and γ is the most compressive principal strain rate. The angle between scalar gradient vector and the eigenvector for α strain rate is denoted by θ_α. This term has been shown[10] to be one of the leading order terms in Eq. (2) and also its contribution to this equation has been shown[13,14,22] to be markedly different in premixed flames compared to chemically non-reacting scalar turbulence. Hence, this interaction term is studied after investigating the behavior of principal strain rates in the simulated V and planar flames.

1. PDF of principal strain rates

Figure 14 shows the PDF of the principal strain rates, α, β, and γ, in the statistically one dimensional, planar cases. These strain rates are normalized using δ_L and S_L and the results are shown for $\tilde{c} = 0.2$ and 0.4 from P60 and $\tilde{c} = 0.2$ from P97 flames. The value of $\tilde{c} = 0.2$ is chosen because the heat release rate peaks at this location for the stoichiometric hydrogen-air flames considered in this study. The variations

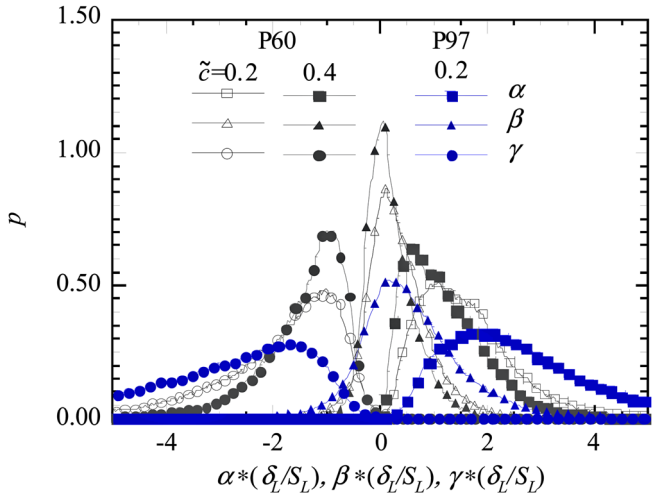

FIG. 14. (Color online) PDF of principal strain rates, normalized using the unstrained planar laminar flame speed and its thermal thickness, for statistically planar one dimensional flames. The results are shown for $\tilde{c} = 0.2$ and 0.4 from P60 and $\tilde{c} = 0.2$ from P97.

shown in Fig. 14 are consistent with previous studies.[22] The normalized mean values, obtained by taking the first moment of these pdfs, are $\langle\alpha^+\rangle = 1.6$, $\langle\beta^+\rangle = 0.34$, and $\langle\gamma^+\rangle = -1.9$ in the flame P60 for $\tilde{c} = 0.2$ and they, respectively, drop to $\langle\alpha^+\rangle = 1.2$, $\langle\beta^+\rangle = 0.21$, and $\langle\gamma^+\rangle = -1.4$ because of the compounded effects of turbulence decay and a reduction in the heat release rate. The sum of these three averaged principal strain rates will be non-zero as it represents the locally averaged dilatation and this value is found to be 0.04 and 0.01 at $\tilde{c} = 0.2$ and 0.4, respectively. The larger value of mean dilatation for $\tilde{c} = 0.2$ is because of the maximum heat release rate at this location. The results for P97 flame in Fig. 14 shows that the turbulent strain rates are larger than for P60 flame (see the clear increase in the PDF for larger values of normalized strain rates). The mean values in P97 flame are $\langle\alpha^+\rangle = 2.7$, $\langle\beta^+\rangle = 0.62$, and $\langle\gamma^+\rangle = -3.3$. The sum of these three values gives 0.02, which implies that the local mean dilatation is reduced as the turbulence level is

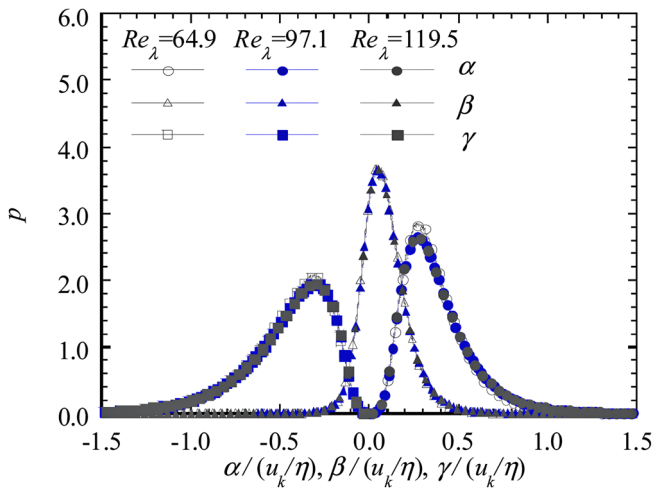

FIG. 15. (Color online) PDF of principal strain rates, normalized using the Kolmogorov scales, in nonreacting flow.

increased. However, it must be noted that it is non-zero and thus the flame surface cannot be treated as a passive interface as has been assumed in some combustion modeling approaches and earlier analyses.

The PDFs shown in Fig. 15 is for non-reacting homogeneous isotropic turbulence inside a cubic domain for three different values of turbulence Reynolds number based on Taylor micro-scale. For these non-reacting cases, the use of Kolmogorov scales to normalize the principal strain rates collapses the PDFs well. The use of neither the Kolmogorov nor the planar laminar flame scales collapse the strain rate PDFs in the turbulent flames considered here. This clearly suggests that it may not be possible to have a single time scale which can be used to scale the principal strain rates in turbulent flames because of the competing effects of small scale turbulence and the local thermo-chemical processes.

Figure 16 shows the PDFs of normalized principal strain rates from V60 and V60H flames. Typical results are shown for $\tilde{c} = 0.3$ at locations x_2, x_3, and x_4 for the V60 case in Fig. 16(a) and for three different values of $\tilde{c}$ at one streamwise location x_2 for the V60H case. The averaged values of the normalized principal strain rates are $\langle\alpha^+\rangle = 3.9$ and $\langle\gamma^+\rangle = -4.3$ at x_2, $\langle\alpha^+\rangle = 3.6$ and $\langle\gamma^+\rangle = -3.3$ at x_3, and $\langle\alpha^+\rangle = 2.2$ and $\langle\gamma^+\rangle = -4.4$ at x_4. The value of $\langle\alpha^+\rangle$ is decreasing gradually along the streamwise direction, whereas $|\langle\gamma^+\rangle|$ decreases first and then increases. These

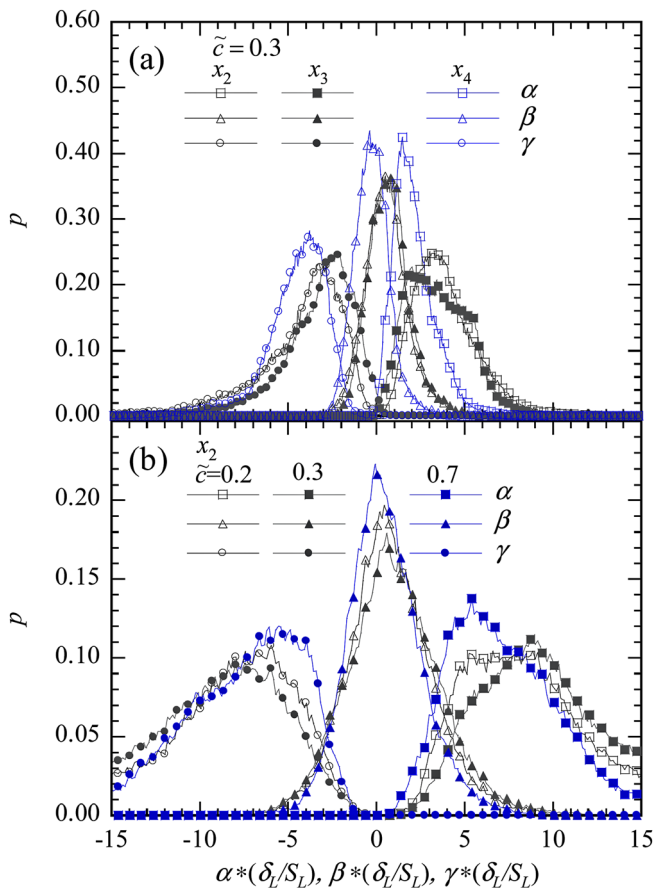

FIG. 16. (Color online) PDF of principal strain rates in V60 (a) and V60H (b) cases. The location of sampling volume is: x_2, x_3, and x_4 for V60, and x_2 for V60H. Progress variable is: $\tilde{c} = 0.3$ for V60, and $\tilde{c} = 0.2$, 0.3 and 0.4 for V60H.

behaviors are due to the compound effects of turbulence production and heat release from the flame. If the turbulence decays with downstream distance as in the case of grid turbulence then the values of these averaged strain rates are expected to decrease. In the V-flame configuration considered here, the turbulence does not simply decay because of its production via the shear as noted in Fig. 5, and thus the averaged values of these strain rates are expected to increase if there are no other competing effects. However, the heat release from the flame creates an extensive strain rate locally which opposes the effects of the compressive strain. Thus, in the near field region where the heat release is strong (see the reaction rate contours in Fig. 11) the value of $|\langle\gamma^+\rangle|$ decreases with streamwise distance. Since the heat release is small and the turbulence generation continues, the average value of the compressive strain increases and is also larger than $\langle\alpha^+\rangle$ as suggested[48] by the classical pictures of turbulence. The effect of flow geometry can also be seen by comparing Figs. 14 and 16(a), which shows that the most probable principal strain rates in V60 flame are about twice as large as in P60 flame even though the turbulence level at inflow boundary is the same for these two cases. This difference is due to the presence of mean shear in the V-flame configuration as one would expect and discussed in Sec. III A 1.

The PDFs of normalised principal strain rates from the flame V60H are shown in Fig. 16(b) for $\tilde{c} = 0.2$, 0.3, and 0.7 at x_2. This figure address the typical variation of these PDFs across the shear layer, since $\tilde{c}$ varies with y/d as shown in Fig. 4. These three values are chosen to represent the thermal region, high heat release region and a region close to the burnt side, see Figs. 4 and 11. Also, one notes from Figs. 5(b) and 5(c) that the turbulence quantities, $\tilde{k}$ and $\tilde{\varepsilon}$, reach their maximum values at about $\tilde{c} = 0.3$. Hence, the strain rate values are large for this value of $\tilde{c}$ in Fig. 16(b). A comparison of Figs. 16(a) and 16(b) clearly shows a significant increase in the PDFs of α and γ strain rates when their magnitudes are larger than 5. Furthermore, the average values of these strain rates for $\tilde{c} = 0.3$ are $\langle\alpha^+\rangle = 10.3$ and $\langle\gamma^+\rangle = -10.6$ in the V60H flame at x_2. These are nearly 2.5 times the values for the V60 flame and this increase is because of the increase in the mean shear due to the change in the incoming mean velocity as noted in Table I. The values of Da and Ka given in Table I clearly suggests that the observed differences in Figs. 14, 16(a), and 16(b) are mainly due to fluid dynamic effect, which is the turbulence production via shear. The effect of heat release is clearly evidenced in Fig. 16(b) by the decrease in the most probable value of α when $\tilde{c}$ is changed from 0.3 to 0.7. This shift is nearly twice larger than the shift of the most probable γ. The behavior of these PDFs in the V97 flame is observed to be very similar to that shown for the V60 case.

2. Alignment of scalar gradient with principal strain rates

From Eq. (12), it is clear that alignments of scalar gradient with the principal strain rates influences the turbulence-scalar interaction term T_{32}. In high Da condition, flame normal aligns with the most extensive strain rates due

to the overwhelming effect of dilatation compared to turbulence.[13] This alignment is also observed in regions of intense heat release in low Da flames[14] simulated in statistically planar and one dimensional configuration using a single irreversible reaction with high activation energy. This alignment behavior is also seen in laboratory scale bluff body stabilized turbulent hydrocarbon flames.[22] Since the stoichiometric hydrogen-air flame does not have high activation energy and has a broader reaction zone, it is of interest to study the flame alignment with the principal strain directions. The statistically planar and V-flames are compared to address the influence of flame geometry.

Figure 17 shows typical variation of flame alignment PDFs for $\tilde{c} = 02 - 04$ in P60 and $\tilde{c} = 0.2$ for P97 flames. These PDFs show a contrasting behavior compared to high Da flames; the gradient of progress variable aligns with the most compressive strain rate even for $\tilde{c} = 0.2$ where the mean reaction rate is noted to be large (for example, see Fig. 11). There are two reasons for this. The first one is related to the competing effects of turbulence and dilatation caused by the heat release. The local dilatation normalized by the large scale turbulence time scale is written as $\nabla \cdot \mathbf{u} = \tau \mathrm{Da}_{\mathrm{L}}$, where τ is the heat release rate parameter and Da_{L} is the local Damkohler number. As noted in Fig. 13, the local Da is smaller than unity and also a close analysis of local temperature variation suggests that $\tau \leq 2$. Typical values of τ are in the range of 6 to 8. The low value of τ and Da_{L} clearly suggests that the heat release effects are weak compared to turbulence in the hydrogen flames considered here, leading to the alignment with the most compressive strain. The second reason is because of the low activation energy of the stoichiometric hydrogen flame leading to a broad reaction zone which also reduces the local impacts of heat release. However, if this alignment is conditioned on the local heat release rate then the alignment of the flame normal with the extensive strain rate becomes apparent as one shall see later, which concurs many of the earlier findings on this attributes of turbulent premixed flames.

Figure 18 shows the PDFs of flame normal alignment with the principal strain rates in the V-flames. The results are shown for V60, V60H, and V97 flames, respectively, in Figs. 18(a)–18(c). The alignment PDF is shown for two streamwise locations, x_1 and x_3, in the regions of high heat release in the V60 case. At x_1, the variation of the alignment PDF differs from that of planar cases by the presence of the distinct peak around $|\cos\theta_\alpha| \approx 0.6$ and $|\cos\theta_\gamma| \approx 0.8$. These peaks are because of the presence of mean shear as it has been noted by Ashurst *et al.*[48] for non-reacting turbulent shear flows. The local Da and τ are noted to be small for the flames simulated here and thus the effects of turbulence overwhelms the heat release effects in general. Since the mean shear decreases with downstream positions, the alignment PDF at x_3 is similar to that shown for the statistically planar case. The results shown for V60H case are similar except for the peaks. The larger peak in V60H case is

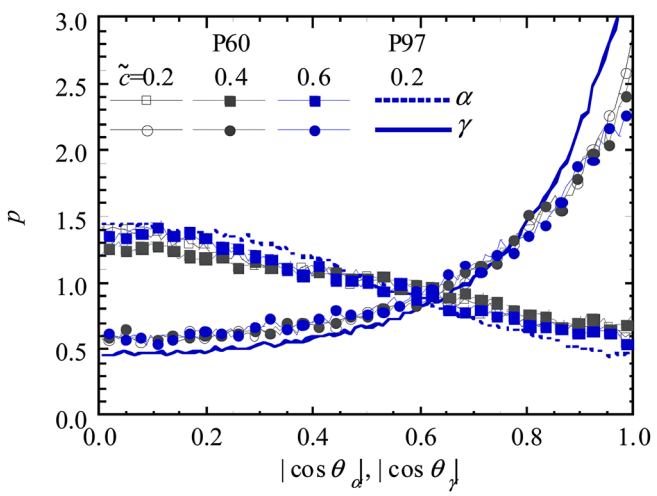

FIG. 17. (Color online) PDF of flame normal alignment with principal strain rates in P60 and P97.

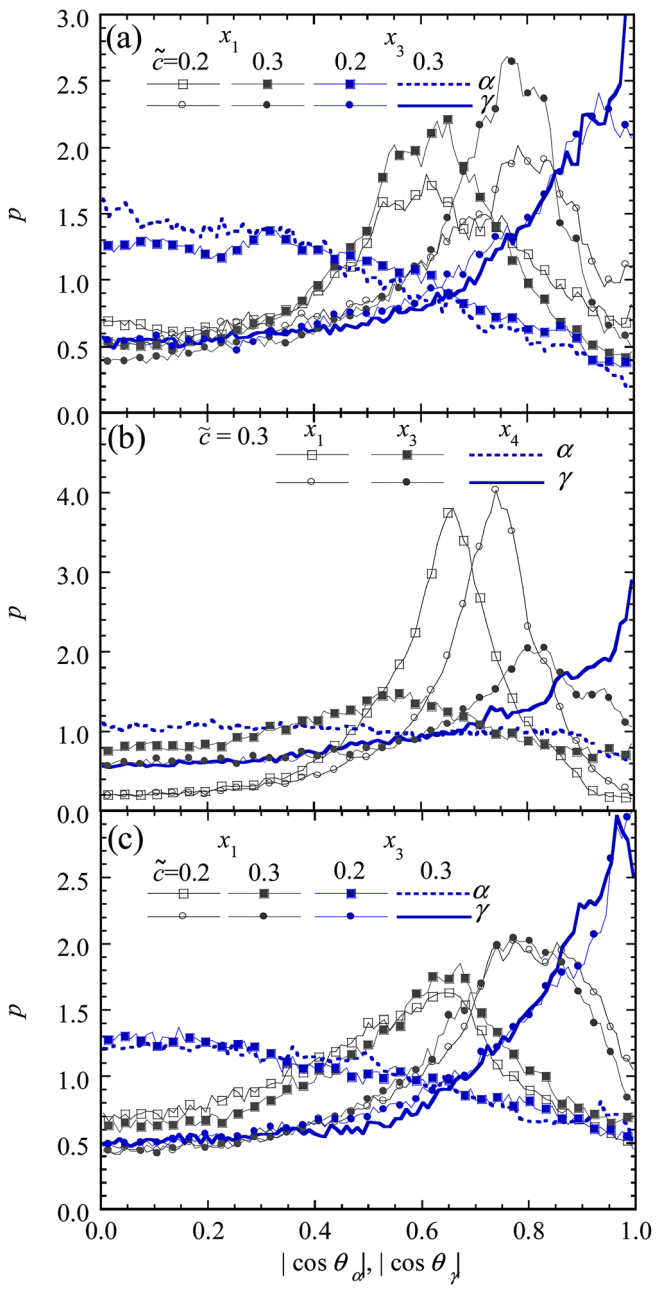

FIG. 18. (Color online) PDF of flame normal alignment with principal strain rates. (a): V60, (b): V60H, (c): V97.

because of the stronger shear produced due to the high incoming mean velocity, $U_{av,}$ at the inlet. It is also evident that the shear effects prevail even at the downstream location x_3 in V60H compared to V60 or V97 flames. Although V97 flame has the same U_{av} as V60H, the effect of mean shear is dominated by the effects of incoming turbulence which is about three times larger. The PDFs from V97 flame shown in Fig. 18(c) is similar to that shown in Fig. 17 for the P97 flame.

3. Alignment PDFs conditioned on heat release rate

The PDF of flame normal alignment with the principal strain rates in Sec. III C 2 shows the effect of shear clearly and the alignment with the most extensive principal strain rate seen in high Da flames is not observed. As described above, a predominant alignment with the most extensive strain rate is caused by intense heat release rate. Thus, in order to see if such conditions also occur locally in the hydrogen flame considered here, the PDFs of flame alignment conditioned on the local heat release rate, $p(\cos\theta|\dot{Q})$, are studied.

Figure 19 shows the conditional PDF, $p(\cos\theta_i|\dot{Q})$, of flame normal alignment with the most extensive and compressive principal strain rates for all the flames considered in this study. The top row (a-f) shows the conditional PDFs for the extensive strain and the bottom row (g-l) is for the compressive strain. The conditioning quantity, heat release rate, is normalized using the maximum heat release rate, $\dot{Q}_{L,max}$, observed in the stoichiometric hydrogen-air laminar premixed flame which propagates freely. The conditional PDF of planar cases, P60 and P97 flames in $\tilde{c} = 0.2$ are shown in the first two columns of Fig. 19 and the rest of this figure shows the conditional PDF for the V-flames at $\tilde{c} = 0.2$. For V60 and V97 flames, the results are shown for location x_2 whereas for the flame V60H two locations, x_2 and x_4 are considered. In all the cases, there are samples with $\dot{Q}/\dot{Q}_{L,max} > 1$ and this is because of preferential diffusion effects.

The conditional PDF of P60 flame shows flame normal preferentially aligning with the most extensive strain rates when the heat release rate is intense, $\dot{Q}/\dot{Q}_{L,max} \geq 0.6$. In the top row, one observes a reasonably good correlation between the heat release rate and the alignment angle, supporting previous findings.[13,14,21,22] However, this correlation is somewhat weak in P97 and V97 cases, compared to other flames, because of relatively lower Da.

In Sec. III C 2, the alignment characteristics in V-flames are shown to be influenced by the mean shear and also similar to the planar flame results when the shear effects diminish. In order to see the competing effects of shear and the heat release rates locally, the spatial locations shown in Fig. 19 for the V-flames are chosen carefully. In the V60 flame, some correlation between the heat release rate and alignment with the extensive strain rate is evident in Fig. 19(c), despite a strong peak near $|\cos\theta_\alpha| \approx 0.5$. This peak is predominantly due to the mean shear. The correlation is clearer in V60H and V97 flames. The mean shear is strong at location x_2 in the V60H flame which reduces the correlation as in Fig. 19(d). Since the mean shear decrease with downstream distance, the variation of the conditional PDF at location x_4 in V60H is similar to that of V60 or planar flames. Without the shear effect, flame normal preferentially aligns with the most extensive strain rates at intense heat release area. The conditional PDF is shown in Fig. 19(f) for V97 flame. As described in Sec. III C 2, the shear loose its effect against turbulent strain rates in V97 flame, which has the highest turbulence intensity among all cases considered for this study. Thus, the effect of shear is reduced in the conditional PDF of the flame alignment (Fig. 19(f)). It must also be noted that the peak in the conditional PDF for $\cos\theta_\gamma$ for $\dot{Q}/\dot{Q}_{Lmax} > 1.0$ is due to the limited sample size in the DNS.

The subtle changes noted in the alignment characteristics must be considered carefully while constructing subgrid models for combustion or scalar mixing in turbulent flows, since these attributes drive the dynamics behind the scalar mixing and thus combustion.

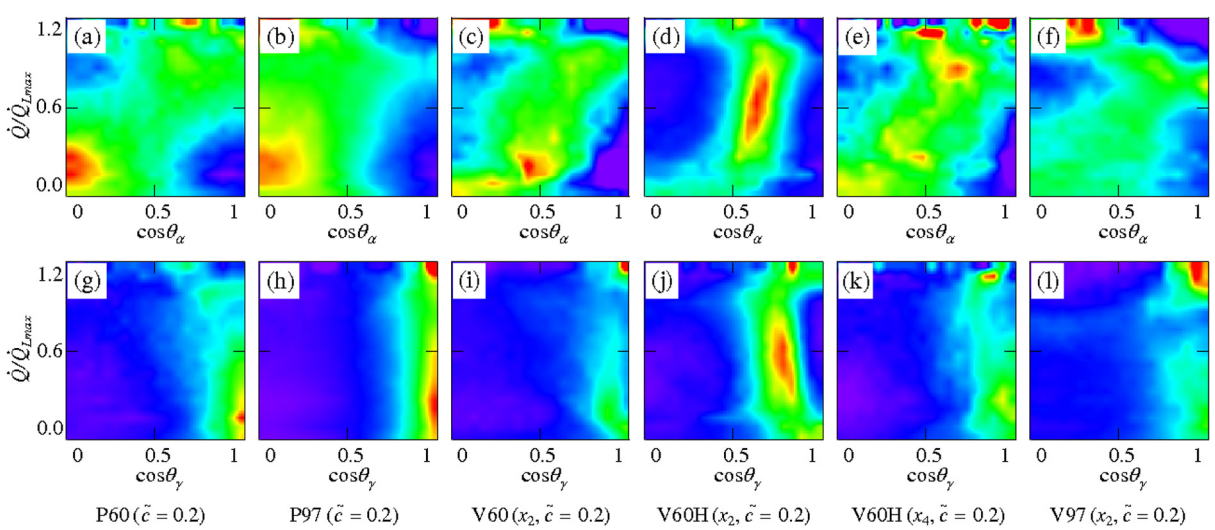

FIG. 19. (Color online) Conditional PDF of flame normal alignment with principal strain rates $p(\cos\theta_\alpha|\dot{Q}/\dot{Q}_{Lmax})$ (top row) and $p(\cos\theta_\gamma|\dot{Q}/\dot{Q}_{Lmax})$ (bottom row).

D. Turbulence-scalar interaction term, T_{32}

In Secs. III C 1 and III C 3, the effect of the balance between turbulence decay and production of turbulence due to the mean shear on the principal strain rates and their alignment with flame normal is explained. This geometry effect is also seen in the variation of T_{32} term shown in Figs. 20(a) and 20(b). The values of T_{32} in V60H case increase with the streamwise distance until $x = x_3$ and then decreases, which is consistent with the behaviour of $\tilde{k}$ and $\tilde{\varepsilon}$ shown in Figs. 5(b) and 5(c). The interaction term is shown for V60 case only at x_1 and for other locations it is much smaller than that shown here. However, T_{32} in V60 case is small compared to V60H. This is because the local turbulence level, produced by the mean shear, is large in V60H compared to V60 as indicated by $\tilde{k}$ and $\tilde{\varepsilon}$ in Fig. 5. The planar case, P60 shows substantially smaller T_{32} than the V-flame cases, although the same level of turbulence is fed from the inlet. In the planar cases, turbulence simply decays, while there is turbulence production via shear in the V-flame cases (the production is more significant in V60H than in V60). Thus the mean shear has a strong indirect influence on the magnitude of T_{32} but not the general features of T_{32} variation with $\tilde{c}$.

In V97 case, T_{32} generally decreases as one moves in the downstream direction. This is because the local increase in the turbulence through the shear production mechanism is not large compared to the shear-free turbulence coming from the inlet as shown in Fig. 5(b). However, the influence of local turbulence on T_{32} magnitude is reinforced by the results in Fig. 20(b) shown for V97 and P97 cases. This can be seen clearly just by comparing P60 and P97 cases.

A simple model[8,47] for T_{32} is also compared with the DNS results for V60H and V97 cases at location x_3 in Figs. 20(a) and 20(b). The model is written as

$$T_{32} \approx [C_3 - C_4 \tau Da_L]\bar{\rho}\tilde{\epsilon}_c\left(\frac{\tilde{\epsilon}}{\tilde{k}}\right), \tag{13}$$

where $C_3 = 15\sqrt{Ka}/(1+\sqrt{Ka})$ and $C_4 = 1.1(1+Ka)^{-0.4}$. It is noted that the model values are multiplied by 20 for both cases. It is clear that the model under-predicts T_{32} for both cases. For V90 case, the multiplied model value shows relatively similar variation to the DNS result compared to V60H case, in which the effect of mean shear is the largest in all the cases (Sec. III A 1). As discussed in Secs. III A 2, III C 1, and III C 3, the mean shear affects the scalar dissipation, while the flame alignment with the principal strain rates does not show the effect of mean shear when the heat release is large. Also, the magnitude of turbulent strain rates is increased by the production of turbulence due to the mean shear. These comparisons of the model and DNS results reinforce above discussions that the flame geometry has significant effect on scalar dissipation rate and the mean shear should be carefully treated in turbulent combustion modelling.

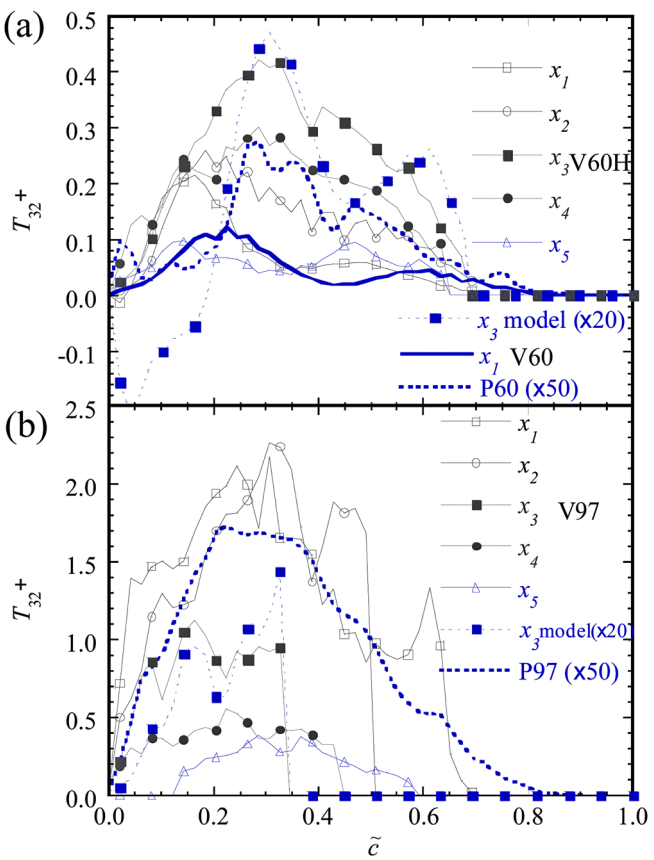

FIG. 20. (Color online) Effect of flame geometry on turbulence-scalar interaction. (a): $Re_\lambda = 60.8$ cases, (b): $Re_\lambda = 97.1$ cases. Note that the values are multiplied by 50 for planar cases and by 20 for the model.

IV. SUMMARY AND CONCLUSION

The effect of flow geometry and Damköhler number on turbulence-scalar interaction has been investigated using direct numerical simulation data. This interaction process is known to be central in scalar mixing[49] and combustion[13,14,21] and this process is represented by the inner product of scalar gradient and the turbulent strain rate. The burning rate is closely related to the mean scalar dissipation rate, which is strongly influenced by the turbulence-scalar interaction as noted in Eq. (2). It has been suggested[19,20] that flame geometry is one of the factors affecting the burning rate in turbulent premixed flames via the flame wrinkling mechanism. Thus, the influence of the flame geometry on the turbulence-scalar interaction is addressed in this study using DNS data of five turbulent, stoichometric hydrogen-air premixed flames in two flame configurations, viz., statistically planar flames and V-flames. The combustion kinetics is simulated using a complex chemical scheme involving 27 elementary reaction and 12 reactive species. The turbulence Reynolds number based on Taylor micro-scale at the inflow boundary for the two statistically planar flames P60 and P97 are 60 and 97, respectively. For the two V-flames, V60 and V60H, this Reynolds number is 60 and the flame V60 has an average incoming velocity of $10S_L$, where S_L is the unstrained planar laminar flame speed. For the V60H and V97 flames, the incoming velocity is twice large and the Taylor micro-scale Reynolds number for the V97 flame is 97. The local combustion conditions in P60 flame is in the border of the corrugated and thin reaction zone regime in a turbulent combustion regime diagram,[41] whereas the conditions in the P97 flame is in the thin

reaction zones regime. The most part of the V-flames are in the thin reaction zones regime.

The analysis of instantaneous flame front structure in the progress variable space suggests a non-flamelet type combustion, however, a time and spatially (along the homogeneous direction) averaged flame front structure is close to unstrained planar laminar flame structure at downstream locations. In the near field regions, the influence of mean strain created by the wake behind the rod is observed to thin the flame leading to conditionally averaged progress variable gradient magnitude nearly 2.5 times larger than the unstrained planar laminar flame values. The spatial variation of flame-brush thickness is observed to follow the Taylor theory of turbulent diffusion when there is no flame-brush interaction and this interaction, which is more likely to occur in practical burners, leads to saturation in the flame-brush thickness variation and it reaches about 5.5 δ_L in the V97 flame.

The principal components of turbulent strain rate are shown to scale with Kolmogorov scale in non-reacting flows and such scaling is not observed for turbulent premixed flames. The most probable strain rate values in V60 are twice larger than in P60. When the mean velocity is increased two times for V60H compared to V60, the magnitude of the most probable principal strain rates increase nearly two times. Furthermore the strain rate PDFs are broader in V60H.

The progress variable gradient is seen to align with the most compressive strain because of low value for the heat release parameter and the local Damkohler number for the flames considered here when the effect of mean shear is small. The most probable alignment angle for the compressive strain is observed 40° and for the extensive strain is 50° when the shear effects are non-negligible (for example, at locations x_1 and x_2 in V-flames considered here). However, an alignment with the most extensive strain is noted in the regions of intense heat release as has been observed in many earlier studies.[13,14,21,22] Also, by comparing the V-flame results to planar flame results for a given turbulence conditions, the effect of flame geometry on the turbulence-scalar interaction process is studied and this interaction effect is observed to be negligible.

Despite the same level of turbulence at the inlet for the planar and V-flames, the presence of mean shear in the V-flames increases the magnitude of T_{32}, the turbulence-scalar interaction term, nearly by two orders of magnitude, when P60 and V60 flames are compared. In V97 flame has the same inlet mean velocity as V60H, but with higher turbulence level, the magnitude of T_{32} is five times larger than in V60H and it decreases generally as one moves in the downstream direction whereas in V60H it increases first and then decreases. This is because the shear production of turbulence in V97 is small compared to the turbulence level in the incoming stream. Thus the magnitude of T_{32} is governed by the local turbulence level which is influenced significantly by the presence of mean shear. However, the general shape of T_{32} variation across the flame-brush is not influenced by the mean shear. A simple model for T_{32} involving the local turbulence and thermo-chemical correlations is also tested. The validation of models will be addressed in future work.

ACKNOWLEDGMENTS

This research is partially funded by the Cabinet Office, Government of Japan through its Funding Program for Next Generation World-Leading Researchers (No. GR038). Y.M. and N.S. acknowledge the support of GCOE program at Tokyo Tech during the summer of 2010. The support of EPSRC by grant EP/F028741/1 is acknowledged by T.D.D. and N.S.

[1]K. N. C. Bray, "The interaction between turbulence and combustion," Proc. Combust. Inst. **17**, 223 (1979).
[2]P. A. Libby and K. N. C. Bray, "Implications of the laminar flamelet model in premixed turbulent combustion," Combust. Flame **39**(1), 33 (1980).
[3]J. W. Rogerson and N. Swaminathan, "Correlation between dilatation and scalar dissipation in turbulent premixed flames," in *Proceedings of the European Combustion Meeting*, Belgium, 2007, pp. 111–136.
[4]N. Chakraborty and N. Swaminathan, "Effetcs of Lewis number on scalar variance transport in premixed flames," Flow, Turbul. Combust. **87**, 261 (2011).
[5]T. Mantel and R. Borghi, "A new model of premixed wrinkled flame propagation based on a scalar dissipation equation," Combust. Flame **96**, 443 (1994).
[6]A. Mura and R. Borghi, "Towards an extended scalar dissipation equation for turbulent premixed combustion," Combust. Flame **133**, 193 (2003).
[7]D. Veynante and L. Vervisch, "Turbulent combustion modeling," Prog. Energy Combust. Sci. **28**, 193 (2002).
[8]H. Kolla, J. W. Rogerson, N. Chakraborty, and N. Swaminathan, "Scalar dissipation rate modeling and its validation," Combust. Sci. Technol. **181**, 518 (2009).
[9]H. Kolla, J. W. Rogerson, and N. Swaminathan, "Validation of a turbulent flame speed model across combustion regimes," Combust. Sci. Technol. **182**, 284 (2010).
[10]N. Swaminathan and K. N. C. Bray, "Effect of dilatation on scalar dissipation in turbulent premixed flames," Combust. Flame **143**, 549 (2005).
[11]N. Chakraborty and N. Swaminathan, "Effects of Lewis number on scalar dissipation transport and its modeling in turbulent premixed combustion," Combust. Sci. Technol. **182**, 1201 (2010).
[12]E. S. Richardson, R. Sankaran, R. W. Grout, and J. H. Chen, "Numerical analysis of reaction-diffusion effects on species mixing rates in turbulent premixed methane-air combustion," Combust. Flame **157**, 506 (2010).
[13]N. Swaminathan and R. W. Grout, "Interaction of turbulence and scalar fields in premixed flames," Phys. Fluids **18**, 045102 (2006).
[14]N. Chakraborty and N. Swaminathan, "Influence of Damköhler number on turbulence–scalar interaction in premixed flames. I. Physical insight," Phys. Fluids **19**, 045103 (2007).
[15]N. Chakraborty, J. W. Rogerson, and N. Swaminathan, "A priori assessment of closures for scalar dissipation rate transport in turbulent premixed flames using direct numerical simulation," Phys. Fluids **20**, 045106 (2008).
[16]N. Chakraborty, J. W. Rogerson, and N. Swaminathan, "The scalar gradient alignment statistics of flame kernels and its modelling implications for turbulent premixed combustion," Flow Turbul. Combust. **85**, 25 (2010).
[17]A. Mura, K. Tsuboi, and T. Hasegawa, "Modelling of the correlation between velocity and reactive scalar gradients in turbulent premixed flames based on DNS data," Combust. Theory Modell. **12**(4), 671 (2008).
[18]A. Mura, V. Robin, M. Champion, and T. Hasegawa, "Small scale features of velocity and scalar fields in turbulent premixed flames," Flow Turbul. Combust. **82**, 339 (2009).
[19]R. W. Bilger, S. B. Pope, K. N. C. Bray, and J. Driscoll, "Paradigms in turbulent combustion research," Proc. Combust. Inst. **30**, 21 (2005).
[20]J. F. Driscoll, "Turbulent premixed combustion: Flamelet structure and its effect on turbulent burning velocities," Prog. Energy Combust. Sci. **34**, 91 (2008).
[21]S. H. Kim and H. Pitsch, "Scalar gradient and small-scale structure in turbulent premixed combustion," Phys. Fluids **19**, 115104 (2007).
[22]G. Hartung, J. Hult, C. F. Kaminski, T. W. Rogerson, and N. Swaminathan, "Effect of heat release in turbulence and scalar-turbulence interaction in premixed combustion," Phys. Fluids **20**(9), 035110 (2008).
[23]A. Mura and M. Champion, "Relevance of the Bray number in the small-scale modeling of turbulent premixed flames," Combust. Flame **156**, 729 (2009).

[24]N. Chakraborty, M. Klein, and N. Swaminathan, "Effects of Lewis number on the reactive scalar gradient alignment with local strain rate in turbulent premixed flames," Proc. Combust. Inst. **32**, 1409 (2009).
[25]E. Gutheil, G. Balakrishnan, and F. A. Williams, in *Lecture Notes in Physics: Reduced Kinetic Mechanisms for Applications in Combustion Systems*, edited by N. Peters and B. Rogg (Springer Verlag, New York, 1993), pp. 177–195.
[26]R. J. Kee, G. Dixon-Lewis, J. Warnatz, M. E. Coltrin, and J. A. Miller, A Fortran computer code package for the evaluation of gas-phase multicomponent transport properties, Sandia National Laboratories Report No. SAND86-8246, 1986.
[27]R. J. Kee, F. M. Rupley, and J. A. Miller, "Chemkin-II: A Fortran chemical kinetics package for the analysis of gas phase chemical kinetics," Sandia National Laboratories Report No. SAND89-8009B, 1989.
[28]M. Tanahashi, M. Fujimura, and T. Miyauchi, "Coherent fine scale eddies in turbulent premixed flames," Proc. Combust. Inst. **28**, 529 (2000).
[29]M. Tanahashi, Y. I. Y. Nada, and T. Miyauchi, "Local flame structure in the well-stirred reactor regime," Proc. Combust. Inst. **29**, 2041 (2002).
[30]Y.-S. Shim, S. Tanaka, M. Tanahashi, and T. Miyauchi, "Local structure and fractal characteristics of H_2-air turbulent premixed flame," Proc. Combust. Inst. **33**, 1455 (2011).
[31]T. Poinsot and S. K. Lele, "Boundary conditions for direct simulations of compressible viscos flows," J. Comput. Phys. **101**, 104 (1992).
[32]M. Baum, T. J. Poinsot, and D. Thévenin, "Accurate boundary conditions for multicomponent reactive flows," J. Comput. Phys. **116**, 247 (1994).
[33]M. Tanahashi, T. Miyauchi, and J. Ikeda, "Scaling law of coherent fine scale structure in homogeneous isotropic turbulence," in *Proceedings of the 11th Symposium on Turbulent Shear Flow* (Grenoble, France, 1997), Vol. 1, p. 4.
[34]A. Y. Poludnenko and E. S. Oran, "The interaction of high-speed turbulence with flames: Global properties and internal flame structure," Combust. Flame **157**, 995 (2010).
[35]M. J. Dunn, A. R. Masri, and R. W. Bilger, "A new piloted premixed jet burner to study strong finite-rate chemistry effects," Combust. Flame **151**, 46 (2007).
[36]N. Swaminathan, R. W. Bilger, and B. Cuenot, "Relationship between turbulent scalar flux and conditional dilatation in premixed flames with complex chemistry," Combust. Flame **126**, 1764 (2001).
[37]N. Swaminathan and R. W. Bilger, "Scalar dissipation, diffusion and dilatation in turbulent H_2-air premixed flames with complex chemistry," Combust. Theory Modell. **5**, 429 (2001).
[38]B. Bédat and R. K. Cheng, "Effects of buoyancy on premixed flame stabilization," Combust. Flame **107**, 13 (1996).
[39]R. K. Cheng, B. Bédat, and L. W. Kostiuk, "Effects of buoyancy on lean premixed V-flames. Part I. Laminar and turbulent flame structures," Combust. Flame **116**, 360 (1999).
[40]S. Pfadler, F. Dinkelacker, F. Beyrau, and A. Leipertz, "High resolution dual-plane stereo-PIV for validation of subgrid scale models in large-eddy simulations of turbulent premixed flames," Combust. Flame **156**, 1552 (2009).
[41]N. Peters, *Turbulent Combustion* (Cambridge University Press, Cambridge, UK, 2000).
[42]K. N. C. Bray and N. Swaminathan, "Scalar dissipation and flame surface density in premixed turbulent combustion," C. R. Mec. **334**, 466 (2006).
[43]A. N. Lipatnikov and J. Chomiak, "Molecular transport effects on turbulent flame propagation and structure," Prog. Energy Combust. Sci. Chem. **31**, 1 (2005).
[44]G. I. Taylor, "Statistical theory of turbulence. IV. Diffusion in a turbulent air stream," Proc. R. Soc. London, Ser. A **151**, 465 (1935).
[45]A. N. Lipatnikov and J. Chomiak, "Turbulent flame speed and thickness: phenomenology, evaluation, and application in multi-dimensional simulations," Prog. Energy Combust. Sci. Chem. **28**, 1 (2002).
[46]T. D. Dunstan, N. Swaminathan, K. N. C. Bray, and R. S. Cant, "Geometrical properties and turbulent flame speed measurements in stationary premixed V-flames using direct numerical simulation," Flow Turbul. Combust. **87**, 237 (2011).
[47]N. Chakraborty and N. Swaminathan, "Influence of Damköhler number on turbulence–scalar interaction in premixed flames. II. Model development," Phys. Fluids **19**, 045104 (2007).
[48]W. T. Ashurst, A. Kerstein, R. Kerr, and C. Gibson, "Alignment of vorticity and scalar gradient with strain rate in simulated Navier-Stokes turbulence," Phys. Fluids **30**, 2342 (1987).
[49]G. Batchelor, "The effect of homogeneous turbulence on material lines and surfaces," Proc. R. Soc. London, Ser. A **213**(1114), 349 (1952).